

# A Semi-analytic Framework of Population III and Subsequent Galaxy Formation on Ultralarge Cosmological $N$ -body Simulations

TOMOAKI ISHIYAMA<sup>1</sup> AND SHINGO HIRANO<sup>2</sup>

<sup>1</sup>*Digital Transformation Enhancement Council, Chiba University, 1-33, Yayoi-cho, Inage-ku, Chiba, 263-8522, Japan*

<sup>2</sup>*Department of Applied Physics, Faculty of Engineering, Kanagawa University, 3-27-1, Rokukakubashi, Kanagawa-ku, Yokohama-shi, Kanagawa 221-0802, Japan*

## ABSTRACT

We develop a new semi-analytic framework of Population (Pop) III and subsequent galaxy formation designed to run on dark matter halo merger trees. In our framework, we consider the effect of the Lyman-Werner flux from Pop III and II stars and the dark matter baryon streaming velocity on the critical minihalo mass for the Pop III formation. Our model incorporates the Lyman-Werner feedback in a self-consistent way, therefore, the spatial variation of Lyman-Werner feedback naturally emerges. The Pop III mass depends on the properties of a minihalo as reproducing radiative hydrodynamical simulation results. We perform statistical studies of Pop III stars by applying this framework to high-resolution cosmological  $N$ -body simulations with a maximum box size of  $16 h^{-1}$  Mpc and enough mass resolution to resolve Pop III-forming minihalos. A top-heavy initial mass function emerges and two peaks corresponding to the  $H_2$  ( $20 \lesssim z \lesssim 25$ ) and atomic cooling halos ( $z \lesssim 15$ ) exist in the distribution. Supermassive stars can be formed in the atomic cooling halos, and the fractions of such supermassive stars increase with the value of streaming velocity. At least an  $8 h^{-1}$  Mpc simulation box and the self-consistent model for the Lyman-Werner feedback are necessary to correctly model the Pop III formation in the atomic cooling halos. Our model predicts one supermassive star per halo with several  $10^9 M_\odot$  at  $z=7.5$ , which is enough to reproduce a high redshift quasar.

*Keywords:* early universe — dark ages, reionization, first stars — dark matter — methods: numerical

## 1. INTRODUCTION

Population III (Pop III) stars, also recognized as first stars, are the first luminous objects in the Universe. Pop III stars are born in primordial gas within dark matter minihalos with masses ranging from approximately  $10^5$  to  $10^7 M_\odot$ , around 100 million years after the Big Bang (e.g., Haiman et al. 1996; Nishi & Susa 1999; Abel et al. 2002; Yoshida et al. 2003). The mass of Pop III stars is predicted to surpass that of present-day stars (e.g., Omukai & Nishi 1998; Omukai & Palla 2001, 2003; Bromm & Larson 2004) because the cooling via  $H_2$ , which is the dominant coolant for the primordial gas in such early Universe, is insufficient. Cosmological radiation hydrodynamical simulations have been consistently predicting that the Pop III stars are typically very massive (e.g., Abel et al. 2002; Yoshida et al. 2006, 2008; Hosokawa et al. 2011; Susa et al. 2014; Hirano et al. 2014, 2015; Toyouchi et al. 2023).

Understanding the initial mass function (IMF) of Pop III stars is essential because it has a large impact on subsequent various phenomena, encompassing the formation of first galaxies and the seeds of supermassive black holes, the cosmic reionization, and the early metal enrichment of the Universe. Consequently, the IMF can be constrained by observations of high redshift galaxies and active galactic nuclei (AGN; e.g., Inayoshi et al. 2020, for reviews and references therein), and the spatial inhomogeneity of the intergalactic medium (IGM; e.g., Kirihara et al. 2020). In fact, early observations conducted by the James Webb Space Telescope (JWST) indicate a preference for top-heavy IMF (e.g., Harikane et al. 2023).

Multiple different observations can be used to constrain specific models of the Pop III star formation process and the resulting IMF. Fragmentation of circumstellar disks in the vicinity of Pop III stars can arise due to the gravitational instability, giving rise to the birth of massive Pop III binary stars (Sugimura et al. 2020, 2023; Kirihara et al. 2023). These binary stars can evolve into progenitors of binary black holes observable through gravitational waves (e.g., Kinugawa et al.

2014). Low-mass Pop III stars can also form (e.g., Clark et al. 2008; Smith et al. 2011; Clark et al. 2011a,b; Greif et al. 2011, 2012; Machida & Doi 2013; Susa 2013; Susa et al. 2014; Susa 2019; Nishijima et al. 2024), and they could survive beyond the current Hubble, if their mass falls below  $0.8 M_{\odot}$ . They can be detected in the Milky-Way as metal-free or -poor stars. Their abundance can constrain the low-mass Pop III IMF (Hartwig et al. 2015; Ishiyama et al. 2016) and the number density of interstellar objects (Kiriwara et al. 2019).

To facilitate detailed theoretical predictions for these observations, we need to comprehensively understand statistics of Pop III stars at high redshift, such as their abundance (for instance, the number density and the Pop III to II ratio), IMF, star formation rate, spatial distribution, and their redshift evolution. Cosmological hydrodynamical simulations and semi-analytic models on dark matter halo merger trees have been utilized in this effort (e.g., Fialkov et al. 2012; Agarwal et al. 2012; Susa et al. 2014; Hirano et al. 2014, 2015; Visbal et al. 2018, 2020; Tanaka & Hasegawa 2021; Hartwig et al. 2022; Chiaki et al. 2023; Hegde & Furlanetto 2023; Bovill et al. 2024; Feathers et al. 2024; Trinca et al. 2024; Ventura et al. 2024). Nevertheless, previous studies have employed relatively limited spatial volume, typically a few  $h^{-1}\text{Mpc}$  (e.g.,  $3 h^{-1}\text{Mpc}$  for Hirano et al. 2015 and  $2 h^{-1}\text{Mpc}$  for Visbal et al. 2020), thereby constraining the statistical analyses due to the absence of large-scale fluctuations. It is also quite difficult to capture the inhomogeneity of Lyman-Werner (LW) background.

In Ishiyama et al. (2016), we have constrained the low mass Pop III IMF employing a simple semi-analytic model and a high-resolution cosmological  $N$ -body simulation having enough resolution ( $< 10^4 M_{\odot}$ ) tailored for the Pop III-forming minihalos and larger volume ( $8 h^{-1}\text{Mpc}$ ) compared to the others mentioned above. In the present paper, we use a huge cosmological  $N$ -body simulation having an even larger volume ( $16 h^{-1}\text{Mpc}$ ) to perform statistical studies of Pop III stars. This simulation was followed down to  $z = 0$ , demonstrating the stark contrast to simulations used in other semi-analytic models. This allows us to predict observational signals of Pop III stars in the current Milky-Way focusing on the galactic archaeology. We also develop a semi-analytic framework of Pop III and subsequent galaxy formation designed to run on halo merger trees. Motivated by results of radiative hydrodynamical simulations, we model the critical minihalo mass for the Pop III formation, its dependency on the LW flux from Pop III and II sources throughout the entire volume and the dark matter baryon streaming velocity, and Pop III IMF. Our model incorporates LW feedback in a self-consistent way, therefore, spatial information of halos is mandatory.

The spatial inhomogeneities of LW intensity has a big impact on the statistical properties of Pop III and II stars. Fig-

ure 1 shows that the introductory visualization of model results. Compared to the uniform LW background model, the self-consistent model promotes the formation of supermassive Pop III stars (displayed by crosses) and prevents that of less massive stars at later epoch. The resulting initial mass function of Pop III stars significantly differs between both models as shown in the remaining of the paper.

In § 2, we describe the numerical detail of the cosmological simulations employed in this study. § 3 gives the details of a new semi-analytic framework of Pop III formation and subsequent galaxy formation. We present results of model calculations in § 4, and scrutinize the impact of the LW feedback model, as well as the box size of  $N$ -body simulations, on the statistical properties of Pop III and II stars at high redshift. § 5 is dedicated to discussion, and § 6 is for the summary and future prospects. In the Appendix, we scrutinize the impact of the mass resolution on the statistics.

## 2. COSMOLOGICAL $N$ -BODY SIMULATIONS

Hierarchical formation and assembly of dark matter halos are followed with large cosmological  $N$ -body simulations having enough resolution tailored for the formation of Pop III minihalos. Subsequently, we model the formation of Pop III and II stars on the merger trees of halos, employing a semi-analytical approach. The details of our semi-analytic model are expounded upon in § 3.

As a fiducial simulation, we adopt the Phi-4096 simulation (Ishiyama et al. 2021), which was run with  $4096^3$  dark matter particles in a comoving box of  $16 h^{-1}\text{Mpc}$ . The particle mass resolution and the gravitational softening length are  $m_p = 5.13 \times 10^3 h^{-1}M_{\odot}$  and  $\varepsilon = 60 h^{-1}\text{pc}$ , respectively. We additionally performed four smaller simulations to investigate the effect of box size and resolution. Two of them, named M8 and M3, have the same mass and force resolution with Phi-4096, but the box sizes of M8 and M3 are  $8 h^{-1}\text{Mpc}$  and  $3 h^{-1}\text{Mpc}$ , respectively. The box size of  $3 h^{-1}\text{Mpc}$  is also similar to those used in previous works such as Hirano et al. (2015) ( $\sim 3 h^{-1}\text{Mpc}$ ) and (Visbal et al. 2020) ( $\sim 2 h^{-1}\text{Mpc}$ ), enabling easy comparison with each other. The simulation H3 is the highest resolution simulation with  $m_p = 6.41 \times 10^2 h^{-1}M_{\odot}$  and  $\varepsilon = 30 h^{-1}\text{pc}$ . The lowest resolution simulation is named L3 with  $m_p = 1.73 \times 10^4 h^{-1}M_{\odot}$  and  $\varepsilon = 90 h^{-1}\text{pc}$ . This mass resolution is similar to those used in other semi-analytic studies (Magg et al. 2018; Griffen et al. 2018). The initial seed of H3, M3, and L3 is identical. The basic parameters of those simulations are listed in Table 1.

The initial conditions of the Phi-4096 were generated by the publicly available code, MUSIC<sup>1</sup> (Hahn & Abel 2011). Those

<sup>1</sup> <https://bitbucket.org/ohahn/music/>

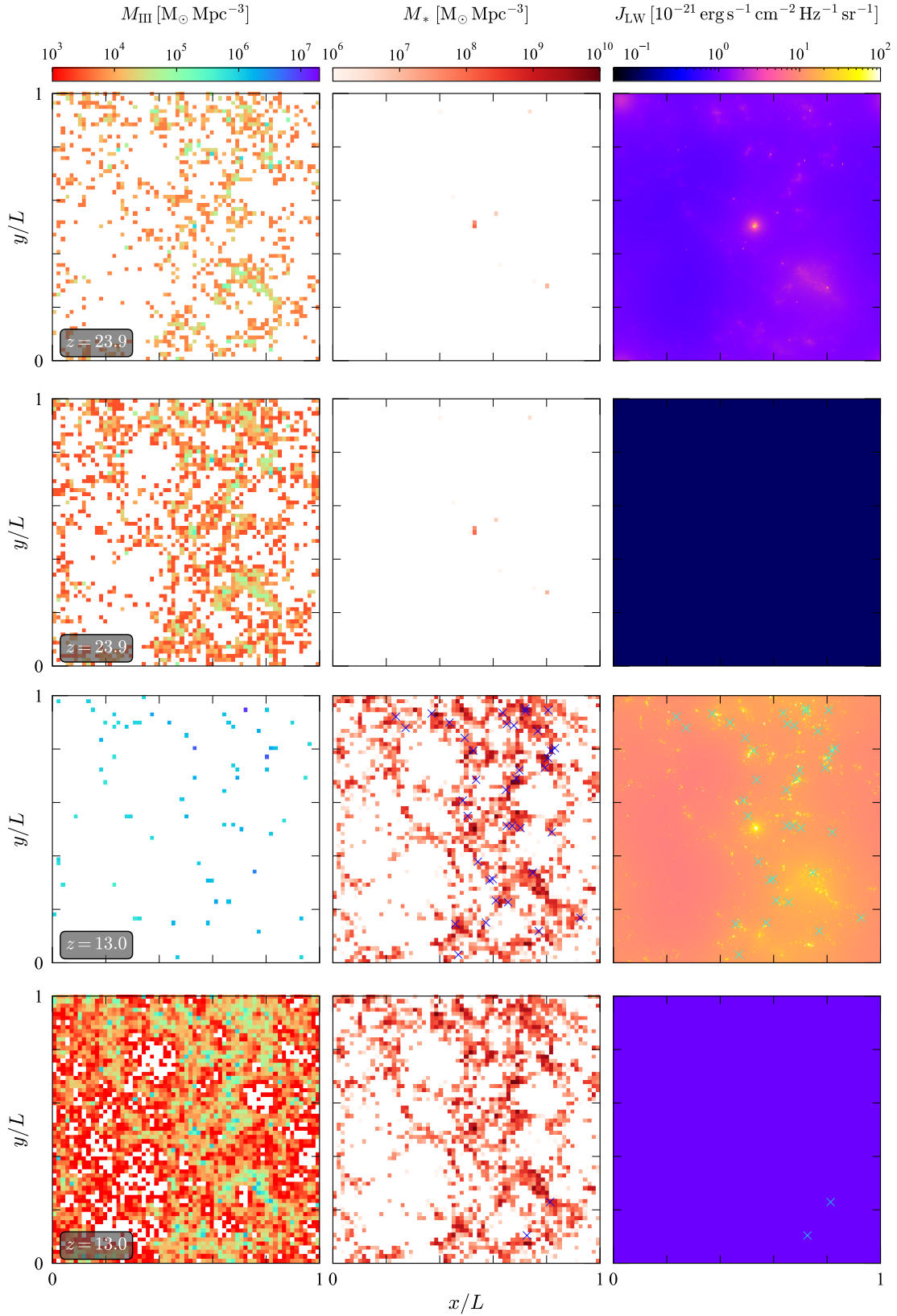


**Figure 1.** Difference of the self-consistent (first and third rows) and the uniform models (second and fourth rows) on the fiducial Phi-4096 simulation ( $L = 16 h^{-1} \text{Mpc}$ ) with zero streaming velocity. Supermassive Pop III stars (more massive than  $10^{4.5} \text{M}_{\odot}$ ) are displayed by crosses. From left to right, each panel shows the spatial distribution of the total mass density of Pop III, Pop II stars, and Lyman-Werner flux, respectively. See also Figure 6.

of all the other simulations were generated by 2LPTIC code <sup>2</sup>. Both codes adopt the second-order Lagrangian perturbation theory (Crocce et al. 2006). We calculated the matter transfer function using the online version of CAMB <sup>3</sup> (Lewis et al. 2000). The cosmological parameters of all simulations are  $\Omega_0 = 0.31$ ,  $\Omega_b = 0.048$ ,  $\lambda_0 = 0.69$ ,  $h = 0.68$ ,  $n_s = 0.96$ , and  $\sigma_8 = 0.83$ , which are consistent with the latest measurement by the Planck Satellite (Planck Collaboration et al. 2020). The initial redshift of all simulations is  $z = 127$ .

The gravitational evolution was followed by a massively parallel TreePM code, GREEM <sup>4</sup> (Ishiyama et al. 2009; Ishiyama et al. 2012) on Aterui II supercomputer at Center for Computational Astrophysics, CfCA, of National Astronomical Observatory of Japan. We accelerated the gravity calculation using PHANTOM-GRAPE<sup>5</sup> code (Nitadori et al. 2006; Tanikawa et al. 2012, 2013; Yoshikawa & Tanikawa 2018). Then, we constructed their merger trees using ROCKSTAR phase space halo/subhalo finder <sup>6</sup> (Behroozi et al. 2013a) and CONSISTENT TREES MERGER TREE CODE <sup>7</sup> (Behroozi et al. 2013b) for the entire volume of all simulations from redshift  $z_{\text{start, mrgt}} \sim 7.5$ , where  $z_{\text{start, mrgt}}$  is the starting redshift of halo/subhalo merger trees. For Phi-4096,  $z_{\text{start, mrgt}} = 43$  when first halos emerge in the merger tree, and for the others,  $z_{\text{start, mrgt}} = 31$ . The number of snapshots stored is 58 between  $z \sim 31$  to  $\sim 7.5$  for all simulations, and the Phi-4096 additionally has 14 snapshots between  $z \sim 43$  to  $\sim 31$ . The snapshot's logarithmic temporal interval  $\Delta \log(1+z)$  is about 0.01.

### 3. SEMI-ANALYTIC MODEL

In this section, we describe our semi-analytic model for the formation of Pop III and II stars, and their Lyman-Werner (LW) radiation, designed to run on the merger histories of dark matter halos taken from cosmological  $N$ -body simulations. In our model, the LW feedback is modelled as a self-consistent way, hence the spatial information of halos is mandatory.

#### 3.1. Sub-stepping

The temporal intervals between global timesteps of merger trees are typically larger than the lifetime of massive Pop III stars. For instance, the intervals of global timesteps are about 6 Myr at  $z = 20$  and 16.6 Myr at  $z = 10$  in our merger trees, exceeding the lifetime of massive stars (1~10 Myr: Schaerer 2002). To track the star formation precisely, we use sub-stepping technique of merger trees. We decompose

each global timestep of merger trees into a constant number of substeps,  $N_{\text{sub}}$ , and randomly assign each halo merger between global timesteps to one of these substeps. We also compute the dark matter smooth accretion mass ( $M_{\text{smooth}}$ ) between global timesteps by subtracting the accumulated mass of all progenitor halos from a given halo, and assume that the smooth mass accretion occurs uniformly across substeps, as expressed by  $dM = M_{\text{smooth}}/N_{\text{sub}}$ .

By default, we set  $N_{\text{sub}} = 50$ . In this case, sub-timesteps are much less than and comparable to the lifetime of a massive star at high and low redshift, respectively. This value also ensures the convergence of Pop III statistics, such as the global star formation rate and the IMF. As described in the following sections, the Pop III formation, the baryon cycling, and the stellar LW feedback are calculated at each substep.

#### 3.2. Condition of Pop III formation

By tracking the merger trees of halos from the highest redshift, we compare the virial mass of each halo  $M_{\text{vir}}$  with a critical value  $M_{\text{crit}}$  that depends on redshift, LW flux, and streaming velocity. We assume a single Pop III stars form in pristine cold dense gas in minihalos with  $M_{\text{vir}} \geq M_{\text{crit}}$ . If any progenitor of a halo experiences preceding Pop III formation, we assume that metal is provided in the given halo and suppresses subsequent Pop III formation in the halo. For  $M_{\text{crit}}$ , we adopt a fitting function based on cosmological hydrodynamical simulations proposed by Kulkarni et al. (2021), which takes the dependency of LW flux on each minihalo, the value of streaming velocity, and redshift into account. This fitting function gives the critical mass  $M_{\text{K21}}$  as

$$M_{\text{K21}}(J_{\text{LW}}, v_{\text{bc}}, z) = M_{z20}(J_{\text{LW}}, v_{\text{bc}}) M_{\odot} \times \left( \frac{1+z}{21} \right)^{-\alpha_{\text{K21}}(J_{\text{LW}}, v_{\text{bc}})}, \quad (1)$$

where,  $J_{\text{LW}}$  and  $v_{\text{bc}}$  are the LW flux on a halo and the streaming velocity in the units of  $10^{-21} \text{ erg s}^{-1} \text{ cm}^{-2} \text{ Hz}^{-1} \text{ sr}^{-1}$  and  $\text{km s}^{-1}$ , respectively.  $M_{z20}$  and  $\alpha_{\text{K21}}$  are functional forms of  $J_{\text{LW}}$  and  $v_{\text{bc}}$  (see Kulkarni et al. 2021 for the detail). In our semi-analytic model, we self-consistently calculate  $J_{\text{LW}}$  on each halo following the procedure described in § 3.5. The value of streaming velocity  $v_{\text{bc}}$  is a model parameter. The typical variance of the streaming velocity is  $\sigma_{v_{\text{bc}}} = 30 \text{ km s}^{-1}$  at the time of recombination, and this is coherent across several comoving Mpc (Tseliakhovich & Hirata 2010; Tseliakhovich et al. 2011), which is smaller than the box size of Phi-4096 simulation. Nevertheless, we assume it is uniform across the entire volume to easily compare how the different values of streaming velocity impact on Pop III statistics.

Kulkarni et al. (2021) studied the critical halo mass using cosmological hydrodynamical simulations with varying  $J_{\text{LW}}$  and  $v_{\text{bc}}$ . However, the maximum values of  $J_{\text{LW}}$  studied by them are 30, 10, and 1 for  $v_{\text{bc}} = 0, 1\sigma_{v_{\text{bc}}}$ , and  $2\sigma_{v_{\text{bc}}}$ , re-

<sup>2</sup> <http://cosmo.nyu.edu/roman/2LPT/>

<sup>3</sup> [http://lambda.gsfc.nasa.gov/toolbox/tb\\_camb\\_form.cfm](http://lambda.gsfc.nasa.gov/toolbox/tb_camb_form.cfm)

<sup>4</sup> <http://hpc.imit.chiba-u.jp/~ishiytm/greem/>

<sup>5</sup> <https://bitbucket.org/kohji/phantom-grape/src>

<sup>6</sup> <https://bitbucket.org/gfstanford/rockstar/>

<sup>7</sup> <https://bitbucket.org/pbehozi/consistent-trees/>

**Table 1.** Parameters of cosmological  $N$ -body simulations used in this study. Here,  $N$ ,  $L$ ,  $\varepsilon$ ,  $m_p$ ,  $z_{\text{fin}}$ , and  $z_{\text{start,mrgt}}$  are the total number of particles, box length, softening length, particle mass resolution, the final redshift of simulations, and the starting redshift of halo/subhalo merger trees, respectively.

Name	$N$	$L (h^{-1}\text{Mpc})$	$\varepsilon (h^{-1}\text{pc})$	$m_p (h^{-1}M_{\odot})$	$z_{\text{fin}}$	$z_{\text{start,mrgt}}$
Phi-4096	$4096^3$	16.0	60	$5.13 \times 10^3$	0.0	43
M8	$2048^3$	8.0	60	$5.13 \times 10^3$	7.5	31
H3	$1536^3$	3.0	30	$6.41 \times 10^2$	7.5	31
M3	$768^3$	3.0	60	$5.13 \times 10^3$	7.5	31
L3	$512^3$	3.0	90	$1.73 \times 10^4$	7.5	31

spectively. We must pay attention when we apply this fitting function to outside of these parameter spaces. In fact, when  $v_{\text{bc}}$  is high, this fitting function provides a smaller critical mass in higher  $J_{\text{LW}}$  ( $> 100$ ) than in smaller  $J_{\text{LW}}$ . This is physically strange but is not surprising because this fitting function was not calibrated for such high  $J_{\text{LW}}$ . To apply this fitting function to such parameter spaces, we modify it as follows,

$$\max_{x \in [0, J_{\text{LW}}]} M_{\text{K21}}(x, v_{\text{bc}}, z) \rightarrow M_{\text{K21}}(J_{\text{LW}}, v_{\text{bc}}, z). \quad (2)$$

This recipe ensures that the critical mass increases monotonically with  $J_{\text{LW}}$ .

As Pop III and subsequent Pop II star formation proceed, UV radiation in the Lyman-Werner bands from these stars photodissociates  $\text{H}_2$  molecules in relatively low mass minihalos and suppresses Pop III formation via  $\text{H}_2$  cooling within the minihalos. If such pristine minihalos are massive enough (virial temperature  $T_{\text{vir}} \gtrsim 8000$  K), atomic hydrogen could be a major coolant and massive Pop III can form (e.g., Omukai & Palla 2001; Bromm & Loeb 2003; Inayoshi et al. 2014; Fernandez et al. 2014; Becerra et al. 2015; Chon et al. 2016). We also follow such massive Pop III formation via atomic cooling by adopting the following criterion of atomic cooling halo, which was employed in Visbal et al. (2020) and Feathers et al. (2024) based on cosmological hydrodynamical simulations of Fernandez et al. (2014),

$$M_{\text{a}} = 5.4 \times 10^7 M_{\odot} \left( \frac{1+z}{11} \right)^{-\frac{3}{2}}. \quad (3)$$

Finally, we use the following expression as a critical minihalo mass of the Pop III formation,

$$M_{\text{crit}} = \min(M_{\text{K21}}, M_{\text{a}}). \quad (4)$$

Figure 2 shows examples of critical halo mass  $M_{\text{crit}}$  of Pop III-forming halos as a function of redshift for  $(J_{\text{LW}}, v_{\text{bc}}) = (0, 0)$ ,  $(10, 0)$ ,  $(100, 0)$ ,  $(0, 1\sigma_{\text{vbc}})$ ,  $(10, 1\sigma_{\text{vbc}})$ , and  $(100, 1\sigma_{\text{vbc}})$ . The critical mass gradually increases with decreasing redshift in any case. The existence of LW flux and streaming velocity further increases the critical mass as expected from their physical nature. The critical mass follows

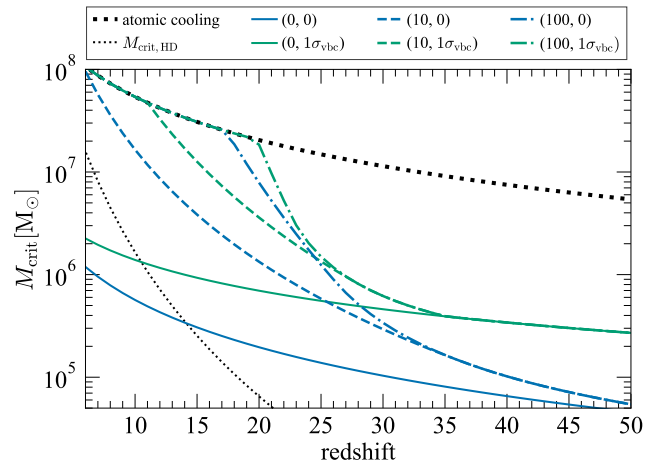


**Figure 2.** Critical halo mass  $M_{\text{crit}}$  of Pop III-forming halos as a function of redshift employed in our semi-analytic model [Eq (4)]. Solid, dashed, and dot-dashed curves indicate examples for various combinations of  $(J_{\text{LW}}, v_{\text{bc}})$ . Upward thick- and downward thin-dotted curves represent the critical mass of atomic cooling halos [Eq (3)] and the critical mass of the HD cooling [Eq (7)], respectively.

the atomic cooling limit [Eq (3)] after redshift when the critical mass described in Eqs. (1) and (2) reaches this limit. This redshift is earlier in the higher streaming velocity model than in the lower one because of the systematically higher critical mass.

### 3.3. Pop III mass

Once the virial mass of a pristine halo exceeds the critical mass  $M_{\text{crit}}$  described in the previous section, we assume that a single Pop III star forms instantaneously in the halo. Note that recent radiative hydrodynamical simulations showed that massive Pop III binary stars can be born as a result of fragmentation of circumstellar disks in the vicinity of Pop III due to the gravitational instability (Sugimura et al. 2020, 2023). We discuss the effect of Pop III multiplicity on our model results in § 5.2.

Previous studies assume that the total mass of Pop III,  $M_{\text{III}}$ , is constant in each halo (Feathers et al. 2024), or is in proportion to the halo mass with a constant star formation efficiency (Visbal et al. 2018, 2020). In the case of Hartwig et al. (2022), a power-law IMF,  $\frac{dN}{d \log M_{\text{III}}} \propto M_{\text{III}}^{-\alpha_{\text{III}}}$ , is used to

assign the masses of Pop III stars in a given halo, where  $\alpha_{\text{III}}$  is a free parameter.

Modern studies based on high-quality radiative hydrodynamical simulations have shown that the mass of Pop III star is affected by physical properties of host halos. Using two-dimensional axisymmetric radiative hydrodynamical simulations of Pop III formation in one hundred halos sampled from cosmological simulations, [Hirano et al. \(2014\)](#) found that the final Pop III stellar mass correlates with the physical properties of the star-forming cloud and host halo, such as the gas infall rate at the Jeans scale,  $\dot{M}_{\text{Jeans}}$ . [Hirano et al. \(2015\)](#) further extended this study and constructed an empirical formula that connects  $\dot{M}_{\text{Jeans}}$  and the evolution of halo virial mass as follows.

$$\dot{M}_{\text{Jeans}} = \begin{cases} 3 \times \dot{M}_{\text{vir}} & (M_{\text{vir}} > M_{\text{crit,HD}}), \\ 0.3 \times \dot{M}_{\text{vir}} & (M_{\text{vir}} < M_{\text{crit,HD}}), \end{cases} \quad (5)$$

where  $\dot{M}_{\text{vir}}$  is the mass accretion rate at virial scale empirically fitted by

$$\dot{M}_{\text{vir}} = 1.1 \times 10^{-3} M_{\odot} \text{yr}^{-1} \left( \frac{1+z}{20} \right)^{3.5} \times \left( \frac{M_{\text{vir}}}{4 \times 10^5 M_{\odot}} \right)^{1.75}, \quad (6)$$

and HD cooling is dominant rather than  $\text{H}_2$  below  $M_{\text{crit,HD}}$ , which is a critical value described as

$$M_{\text{crit,HD}} = 3.5 \times 10^5 M_{\odot} \left( \frac{1+z}{15} \right)^{-5}. \quad (7)$$

Finally, the Pop III mass  $M_{\text{H15,III}}$  is modelled as a function of  $\dot{M}_{\text{Jeans}}$ ,

$$M_{\text{H15,III}} = 250 M_{\odot} \left( \frac{\dot{M}_{\text{Jeans}}}{2.8 \times 10^{-3} M_{\odot} \text{yr}^{-1}} \right)^{0.7}. \quad (8)$$

We adopt this formula as a first approximation of the Pop III mass.

We also implement the supermassive star formation in our semi-analytic model. [Toyouchi et al. \(2023\)](#) performed three-dimensional radiation hydrodynamical simulations and found that supermassive stars can form in atomic cooling halos. When the mass accretion rate is high enough,  $\dot{M}_{\text{vir}} > 10^{-2} M_{\odot} \text{yr}^{-1}$ , nearly ten times more massive Pop III stars could form (estimated from Figure 10 of [Toyouchi et al. \(2023\)](#)). Note that they obtained consistent results with [Hirano et al. \(2014, 2015\)](#) in the case of lower accretion rate,  $\dot{M}_{\text{vir}} < 10^{-2} M_{\odot} \text{yr}^{-1}$ . Hence, we populate a single Pop III star per minihalo following the equation,

$$M_{\text{III}} = \begin{cases} M_{\text{H15,III}} & (\dot{M}_{\text{Jeans}} \lesssim 10^{-2} M_{\odot} \text{yr}^{-1}), \\ 10 \times M_{\text{H15,III}} & (10^{-1} M_{\odot} \text{yr}^{-1} \lesssim \dot{M}_{\text{Jeans}}). \end{cases} \quad (9)$$

For  $10^{-2} < \dot{M}_{\text{Jeans}} < 10^{-1} M_{\odot} \text{yr}^{-1}$ , we assign  $M_{\text{III}}$  by log-linearly interpolating between  $M_{\text{III}} | \dot{M}_{\text{Jeans}} = 10^{-2}$  and  $M_{\text{III}} | \dot{M}_{\text{Jeans}} = 10^{-1}$ .

Once we assign the mass of a Pop III star, we determine the lifetime of the star using a table given by [Schaerer \(2002\)](#), which is based on realistic population synthetic models. We linearly interpolate the table and assume the lifetime of a Pop III star with mass more massive than  $10^3 M_{\odot}$  being the same with that of  $10^3 M_{\odot}$  stars, which is the upper limit of the table. The UV radiation of each Pop III star works with constant intensity within its lifetime (details are given in § 3.5).

### 3.4. Baryon cycle

Once the supernova explosion of a massive Pop III star occurs, metal provided by the star mixes with the remaining pristine gas in the halo. As shown in § 4, the Pop III mass in a minihalo is always predicted to exceed the upper limit mass of the pair-instability supernova ( $\sim 260 M_{\odot}$ ) for  $v_{\text{bc}} \gtrsim 1\sigma_{\text{vbc}}$ , therefore, metal enrichment by the supernova explosion does not occur if we assume the spatially uniform streaming velocity across the entire box and the absence of less massive Pop III stars than the model prediction. However, less massive Pop III stars must form around such massive Pop III stars in principle because the coherent scale of the streaming velocity is several comoving Mpc. Therefore, we assume that these halos are massive enough to accrete nearby less massive minihalos that are already enriched, and the metal enrichment occurs in these halos to take the LW feedback from Pop II into account.

If any progenitor of a halo is a minihalo that experiences preceding Pop III formation, we assume that the subsequent Pop III formation in the given halo is suppressed and the Pop II formation occurs when it grows massive enough for efficient gas cooling. We take a critical value of a minimum virial mass for such Pop II formation halos to be  $M_{\text{th}} = 10^7 M_{\odot}$  as a fiducial value. We model the baryon cycle and the Pop II formation in such halos by largely following a recipe used in [Agarwal et al. \(2012\)](#) and [Chon et al. \(2016\)](#) as follows.

We consider three components of baryonic matter: non star-forming hot gas  $M_{\text{hot}}$ , star-forming cold gas  $M_{\text{cold}}$ , and the total mass of Pop II stars  $M_*$ . We first place  $M_{\text{hot}} = f_{\text{b}} M_{\text{vir}}$  on each halo, where  $f_{\text{b}} = \Omega_{\text{b}}/\Omega_0$ , when they first emerge in the merger trees. Then, we update each component between substeps as follows.

1. *Smooth accretion of gas.* When smooth mass accretion occurs on a halo, the halo also accretes smooth gas. We assume that the gas is heated to the virial temperature, then add  $f_{\text{b}} dM$  to the hot gas component.
2. *Radiative gas cooling.* The radiative cooling of hot gas occurs over the timescale of the halo dynamical time

$t_{\text{dyn}}$ , which is given by

$$t_{\text{dyn}} = \frac{R_{\text{vir}}}{V_c}, \quad (10)$$

$$V_c = 23.4 \left[ \frac{\Omega_0}{\Omega_m(z)} \frac{\Delta_c}{18\pi^2} \right]^{\frac{1}{6}} \left( \frac{M_{\text{vir}}}{10^8 h^{-1} M_\odot} \right)^{\frac{1}{3}} \times \left( \frac{1+z}{10} \right)^{\frac{1}{2}} \text{ km s}^{-1}, \quad (11)$$

where,  $R_{\text{vir}}$  is the halo virial radius,  $V_c$  is the circular velocity,  $\Omega_m(z)$  is the density parameter, and  $\Delta_c = 18\pi^2$  is the critical halo overdensity.

3. *Star formation.* In the metal enriched star-forming cold gas, new Pop II stars are born over the timescale of

$$t_{\text{SF}} = \frac{0.1 t_{\text{dyn}}}{\alpha} \quad (12)$$

(e.g., [Kauffmann et al. 1999](#)), where  $\alpha$  is the star formation efficiency and we set  $\alpha = 0.003$ .

4. *Supernovae feedback.* We assume a part of cold gas is converted into hot gas by supernovae explosions and the rate is in proportion to the star formation rate as

$$\gamma \frac{dM_*}{dt} = \gamma \frac{M_{\text{cold}}}{t_{\text{SF}}}, \quad (13)$$

where

$$\gamma = \left( \frac{V_c}{V_{\text{out}}} \right)^{-\beta} \quad (14)$$

([Cole et al. 1994](#)). We set  $\beta = 1.74$  and  $V_{\text{out}} = 110 \text{ km s}^{-1}$ . This process can be modelled as an outflow where the heated cold gas is removed from the halo ([Agarwal et al. 2012](#)). In our model, we do not consider outflows and simply add the heated cold gas into the hot gas component ([Chon et al. 2016](#)).

The four processes are summarized in the following differential equations.

$$\begin{aligned} \frac{dM_{\text{hot}}}{dt} &= -\frac{M_{\text{hot}}}{t_{\text{dyn}}} + \gamma \frac{M_{\text{cold}}}{t_{\text{SF}}} + f_b \frac{dM_{\text{vir}}}{dt}, \\ \frac{dM_{\text{cold}}}{dt} &= \frac{M_{\text{hot}}}{t_{\text{dyn}}} - (1 + \gamma) \frac{M_{\text{cold}}}{t_{\text{SF}}}, \\ \frac{dM_*}{dt} &= \frac{M_{\text{cold}}}{t_{\text{SF}}}. \end{aligned} \quad (15)$$

We explicitly integrate these equations on each substep. When a halo merger occurs at a certain substep, these three components of the less massive halo are added to those of the more massive halo. We do not follow the evolution of less massive halo at later steps.

### 3.5. Lyman-Werner feedback

As described in § 3.2, once Pop III and II stars form, their UV radiation in the LW bands photodissociates  $\text{H}_2$  molecules in relatively less massive and nearby minihalos and suppresses subsequent Pop III formation via  $\text{H}_2$  cooling within the minihalos. If these halos grow massive enough, they could be a possible site of massive Pop III formation via atomic cooling. How the LW radiation affects the critical mass of Pop III-forming minihalos is given in Eqs. (1) and (2). In this section, we describe how to calculate the LW flux,  $J_{\text{LW}}$ , on each halo.

We adopt a self-consistent model for the LW feedback in which the LW flux on each halo is calculated by accumulating the contributions from all radiative sources of both living Pop III and II stars, resulting in a spatially and time variable treatment. We employ the following equations proposed by [Johnson et al. \(2013\)](#) to compute the contribution from a source on a halo,

$$\begin{aligned} J_{\text{LW,III}} &= 15 \left( \frac{r}{1 \text{ kpc}} \right)^{-2} \left( \frac{M_{\text{III}}}{10^3 M_\odot} \right), \\ J_{\text{LW,II}} &= 3 \left( \frac{r}{1 \text{ kpc}} \right)^{-2} \left( \frac{M_*}{10^3 M_\odot} \right), \end{aligned} \quad (16)$$

where  $r$  is the distance between the centers of the source and the given halo in physical coordinates, where the center is defined as the most bound place in the halo. The first equation gives the LW flux from a Pop III star, while the second one is for a Pop II-forming halo. For  $M_*$ , we instead use the total mass of Pop II stars formed within 5 Myr from the current substep, which is derived by multiplying the instantaneous star formation rate at the substep with this period.

As the Pop III and II formation proceeds, the number of sources increases. Therefore, the direct summation of Eq (16) is impractical because the calculation cost is in proportion to both the number of sources and halos in the merger tree. We accelerate this calculation using Fast Fourier Transformation (FFT) as an approach in [Visbal et al. \(2020\)](#). The periodic boundary condition used in the cosmological simulations is also naturally solved by the FFT. First, we set a uniform grid on the entire volume, where the number of grid points is expressed by  $N_g$  in one dimension. We calculate the source energy (corresponds to a term without  $r^{-2}$  in Eq (16)) from each grid by assigning the energy of all sources nearby the given grid using the CIC (Cloud in Cell) scheme. Then, the LW flux from a grid to all other grids is obtained using the FFT and the convolution with the Fourier transformation of the  $r^{-2}$  kernel. Finally, we calculate the LW flux on each halo by interpolating the flux on the nearby grids.

The method described above is in analogy with the Particle-Mesh (PM) method generally used in gravitational  $N$ -body simulations. To calculate the contribution of nearby sources more precisely, we adopt a method in analogy with the

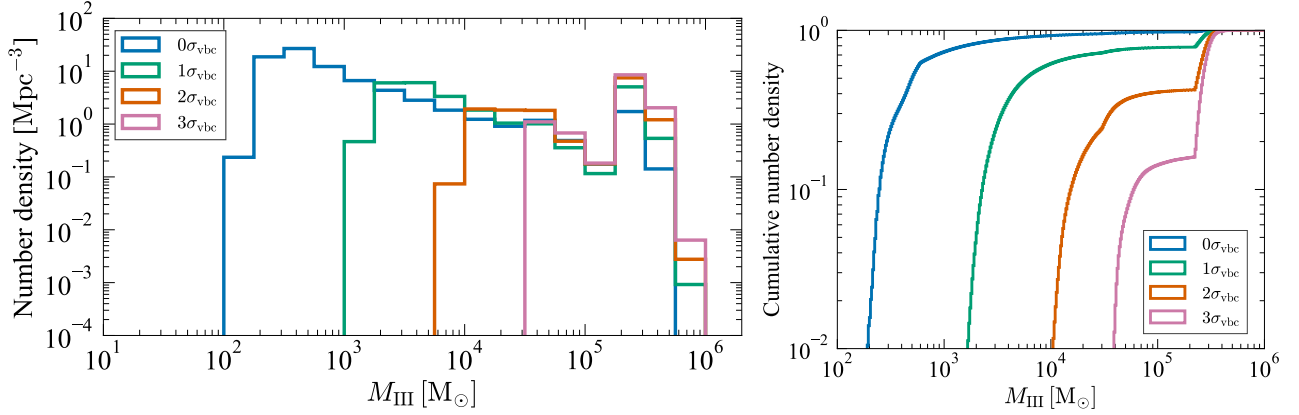


**Figure 3.** (Left) Number density of Pop III stars across redshift as a function of the Pop III mass in a halo. We divide a single-digit mass range into four logarithmic bins and calculate the number density in each bin. Four model results with the different values of streaming velocity,  $v_{bc} = 0, 1\sigma_{vbc}, 2\sigma_{vbc},$  and  $3\sigma_{vbc}$ , are shown. (Right) Cumulative probability distribution of the number of Pop III stars as a function of the Pop III mass in a halo.

Particle-Particle Particle-Mesh ( $P^3M$ ) method, where we introduce the cutoff radius  $r_{cut}$ . The contributions from all sources within the cutoff radius to a halo are computed directly using Eq (16). For the convolution, we set the kernel value to zero from the contributions within the cutoff radius to avoid double counting. We set  $N_g = 512^3, 256^3,$  and  $128^3$  for the simulations with the box size of  $L = 16.0, 8.0,$  and  $3.0 h^{-1}\text{Mpc}$ , respectively, and  $r_{cut} = L/N_g$ . These values ensure the convergence of Pop III statistics.

#### 4. RESULTS

We perform four semi-analytic calculations on the fiducial Phi-4096 simulation with different values of the streaming velocity,  $v_{bc} = 0, 1\sigma_{vbc}, 2\sigma_{vbc},$  and  $3\sigma_{vbc}$ , where  $\sigma_{vbc} = 30 \text{ km s}^{-1}$ . Other model parameters are fixed across four calculations and shown in the previous section. We start the calculations from  $z = 43$  when first halos emerge in the merger tree and follow the evolution until  $z = 7.5$ . In this section, we begin by showing the initial mass function of Pop III across redshift and compare the results between four runs. Then, we compare the star formation history of these runs. We also investigate the effect of box size (§ 4.3) and mass resolution (Appendix A) on statistical results using slim simulations.

##### 4.1. Initial mass function

The left panel of Figure 3 shows the number density of Pop III stars across redshift as a function of the Pop III mass within each halo. In all models, there are no minihalos that contain Pop III with  $M_{III} \lesssim 100 M_\odot$ . The critical halo mass of Pop III-forming halos increases with decreasing redshift, while the mass accretion rate increases with redshift and halo mass as shown in Eq (6). This balance prevents the formation of less massive Pop III stars. The least mass of Pop III increases with the streaming velocity as a natural consequence. In all models, the number density decreases with increasing Pop III mass from the first peak around the less massive

end and has the second peak at  $M_{III} = 10^{(5-6)} M_\odot$ . For  $v_{bc} = 0$ , the first peak is at around several hundred  $M_\odot$ , which is consistent with a large suite of radiative hydrodynamical simulations (Hirano et al. 2015), considering only the  $H_2$  mode. In their simulations, Pop III stars with mass less massive than  $100 M_\odot$  form; however, the formation mode of majority of them is via both  $H_2$  and HD. As described in 3.3, our model takes the HD mode into account. However, the critical mass of the HD mode is always smaller than the Pop III critical mass except for  $z \lesssim 15$  as shown in Figure 2. In fact, a large fraction of less massive Pop III stars form at  $10 \lesssim z \lesssim 15$  in Hirano et al. (2015). After this redshift, the LW background grows sufficiently in our model, and therefore, no less massive Pop III stars are born via HD cooling even in the  $v_{bc} = 0$  case. On the other hand, Hirano et al. (2015) adopted a smaller simulation box ( $3 h^{-1}\text{Mpc}$ ) than our study ( $16 h^{-1}\text{Mpc}$ ), possibly resulting in weaker LW feedback and the formation of less massive Pop III stars.

The second peak corresponds to the atomic cooling halos, where supermassive stars are born. Such second peak is also seen in a semi-analytic study by Toyouchi et al. (2023) for a mass distribution of primordial stars in a high- $z$  progenitor halo of Quasi-Stellar Object (QSO). As shown in Figure 2, the critical halo mass increases with the LW flux, and reaches the atomic cooling limit at  $z \sim 20$  when the LW flux is sufficiently high. The critical mass of the atomic cooling halo does not depend on the value of streaming velocity in our model, hence the Pop III mass formed in atomic cooling halos tends to be similar regardless of the value of streaming velocity. The second peak is higher with the streaming velocity because the existence of the streaming velocity increases the critical halo mass; therefore, there are more pristine massive halos at  $z \sim 20$  in the higher velocity model than in lower one.

The right panel of Figure 3 is another look of the Pop III mass distribution, the cumulative probability of the number



of Pop III stars as a function of Pop III mass. The sharp rise at  $2 \times 10^5 M_\odot$  corresponds to the atomic cooling halos. The fractions of such supermassive stars are about 2, 21, 57, and 83% for  $v_{bc} = 0, 1\sigma_{vbc}, 2\sigma_{vbc},$  and  $3\sigma_{vbc}$ , respectively. These results indicate that the majority of Pop III stars are supermassive in high streaming velocity regions.

Figure 4 demonstrates the dependence of Pop III mass on properties of halos: virial mass, redshift, and LW flux of host halos. All panels exhibit two sequences. In the panel of the virial mass, the number of Pop III has peaks around the lowest Pop III mass. Regardless of the value of streaming velocity, the corresponding redshift and LW flux are around  $20 \lesssim z \lesssim 25$  and  $J_{LW} \lesssim 10$ , respectively. The lowest mass increases with the value of streaming velocity as already seen in Figure 3 because the typical minihalo mass also increases with the value of streaming velocity. The Pop III mass gradually increases with the virial mass because the mass accretion rate also increases. The number density of Pop III mass gradually decreases with the virial mass, but finally reaches second peak, which corresponds to the atomic cooling limit. Because the critical mass of atomic cooling does not depend on the value of streaming velocity in our model, the corresponding virial mass and Pop III mass do not change across the value of streaming velocity, while the number density is higher in the second peak than in the first one for  $2\sigma_{vbc}$  and  $3\sigma_{vbc}$  models as already demonstrated in Figure 3.

The second peaks exist around  $7.5 \lesssim z \lesssim 15$ . As the value of streaming velocity increases, the second peaks emerge from slightly higher redshift and the number density therein also becomes higher. Because the  $H_2$  critical mass also increases with the value of streaming velocity, more halos can enter the atomic cooling limit in higher velocity models, as shown in Figure 2. This is also the reason that the LW flux at the second peak is slightly more broadly distributed in higher velocity models toward the lower value. A large fraction of halos can cool via  $H_2$  in lower velocity models, before the LW flux grows sufficiently. Therefore, they have a smaller number of atomic cooling halos with low LW flux.

#### 4.2. Star formation rate density

Figure 5 shows the star formation rate density (SFRD) of Pop III and II stars and the formation rate density of Pop III-forming halos as a function of redshift for four models. The Pop III formation begins around  $z \sim 40$ , and the rate rises with evolving redshift and reaches the first peak at  $20 \lesssim z \lesssim 25$ . Around this redshift, LW flux sufficiently grows to prevent subsequent Pop III formation as shown in Figure 6, which is the distribution of the LW flux radiated on each Pop III-forming halo (see also Figure 1). Hence, the formation rate stagnates and falls regardless of the model. Then, the formation rate rises again as new supermassive Pop III stars are born in atomic cooling halos. As already seen in previous

Figures, the Pop III formation rate reaches the second peak around  $7.5 \lesssim z \lesssim 15$ , and the peak is on earlier redshift with increasing streaming velocity. In the case of SFRD, it stagnates but does not fall once it reaches the first peak. However, the second peak is also observed as well as the formation rate. These double peaks have not been reported in any literature probably because insufficient computational volume was used (e.g., Visbal et al. 2020) or spatially uniform LW background was assumed (e.g., Hartwig et al. 2022). In fact, a large fraction of Pop III-forming halos shows high LW flux ( $J_{LW} > 100$  at  $z = 13$ ) in our self-consistent model as shown in Figure 6, whereas  $J_{LW} \sim 1$  in the uniform model. In § 4.4, we further scrutinize the impact of the LW feedback model on the statistics

Figure 6 shows that the LW flux is dominated by Pop III sources at earlier epoch and Pop II sources at later epoch, corresponding to the SFRD. As the Pop II SFRD increases, the flux from Pop II increases and the contribution from Pop III becomes sub-dominant, as also indicated by Figure 1. Supermassive stars are born close to where the Pop II stars are concentrated and the LW flux from them is also high. Those pictures and the distribution of the LW flux are broadly consistent with the previous studies (Agarwal et al. 2012; Chon et al. 2016). There is difference in the minimum value of flux from Pop III sources probably due to the adopted Pop III mass model.

The Pop III SFRD is higher with increasing streaming velocity, while the formation rate density of Pop III-forming halos shows the opposite sense in the  $H_2$  cooling regime. These results can be understood as follows. The typical Pop III-forming halo mass increases with the value of streaming velocity; hence, the formation rate of such halos is lower due to the absence of massive halos. In contrast, the Pop III mass increases monotonically with halo mass as already shown in the previous section. The combination of these effects is the cause of this opposite sense. In contrast, in the atomic cooling regime, both the SFRD and Pop III-forming halo formation rate are higher with increasing streaming velocity.

In the Pop II SFRD, we observe no significant difference at  $z \gtrsim 20$  and a slight difference after this redshift between the four models. Throughout the models, the Pop II formation begins on halos that exceed  $M_{th} = 10^7 M_\odot$  and are enriched by other stars. By  $z \sim 20$ , these Pop II-forming halos are easily enriched by Pop III stars regardless of the value of streaming velocity because the Pop III critical mass is always less than  $M_{th}$  until this redshift, as seen in Figure 2 ( $M_{crit} \lesssim 10^6 M_\odot$  at  $z = 20$  and  $J_{LW} = 0$  for  $v_{bc} = 0$  and  $1\sigma_{vbc}$ ) and nearby minihalos should be massive enough to host Pop III stars even for the high  $\sigma_{vbc}$  case due to the nature of halo clustering. Even in the  $3\sigma_{vbc}$  and  $J_{LW} = 0$  case,  $M_{crit} \sim 3 \times 10^6 M_\odot$  is still less than  $M_{th}$ . Consequently, the global Pop II SFRD is similar across the four models. After that redshift, given the high LW

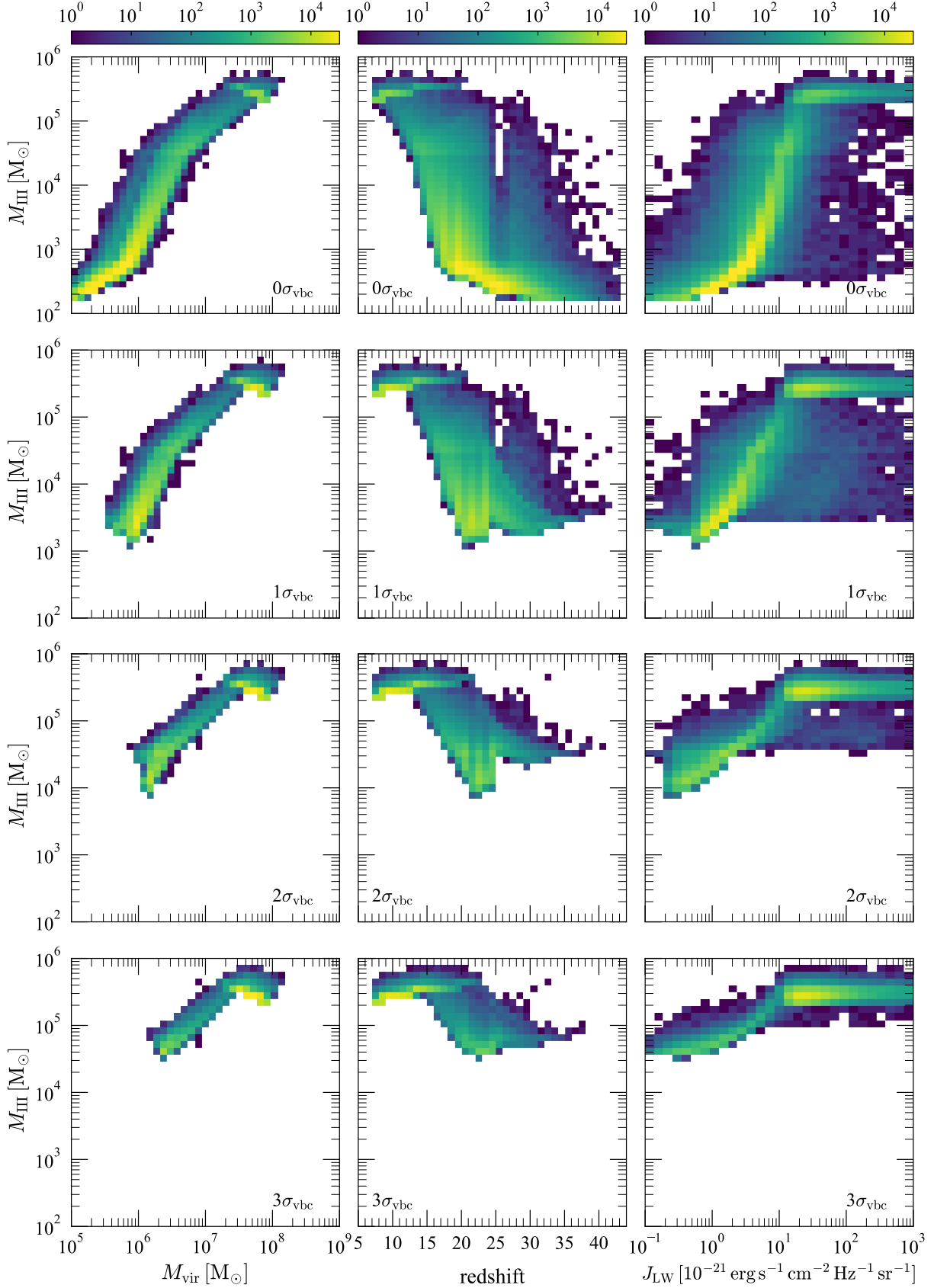


**Figure 4.** Dependence of Pop III mass on virial mass (left), redshift (middle), and Lyman-Werner flux (right) of host halos. From top to bottom, model results with  $v_{\text{bc}} = 0, 1, 2, \text{ and } 3\sigma_{v_{\text{bc}}}$  are presented. Color bars show the number of Pop III stars at each pixel.

intensity, the critical mass rapidly increases with decreasing redshift and the value of streaming velocity, and then finally reaches the atomic cooling mass, which is higher than  $M_{\text{th}}$ . As a result, the contribution to the Pop II SFRD from halos with the mass around  $M_{\text{th}}$  formed at a late time becomes smaller with increasing the value of streaming velocity. This is the reason why the the Pop II SFRD is slightly smaller as the value of streaming velocity increases.

#### 4.3. Box size effect

In this section, we examine the effect of the simulation box size on the Pop III IMF across redshift and SFRD. Figure 7 shows the comparison of model results calculated on simulations with different box sizes (Phi-4096, M8, and M3), which are 16, 8, and  $3 h^{-1}$  Mpc. The results with  $v_{\text{bc}} = 0$  and  $1\sigma_{v_{\text{bc}}}$  are shown in the left and right panels, respectively. In the M3 box, we observe considerably smaller number density of supermassive stars than the Phi-4096 run for both  $v_{\text{bc}} = 0$  and  $1\sigma_{v_{\text{bc}}}$  cases. These are highlighted in the Pop III SFRD plots, not showing the clear second peak for the M3. The Pop II SFRD of the M3 box shows a delay from the others due to the absence of large-scale fluctuations, resulting in insufficient LW feedback from Pop II stars and the suppression of the formation of atomic cooling halos. Correspondingly, the number density of Pop III-forming minihalos increases with decreasing box size due to insufficient LW feedback, as shown in the formation rate plots.

As the box size increases, the number density of supermassive stars increases. In the M8 box, we observe smaller number density of supermassive stars than the Phi-4096 run for the  $v_{\text{bc}} = 0$  case, while it approaches asymptotically to the result of Phi-4096 run for the  $v_{\text{bc}} = 1\sigma_{v_{\text{bc}}}$  case. Those are also highlighted in the Pop III SFRD and the formation rate plots where the second peak in the M8 is weak for  $v_{\text{bc}} = 0$  and appears for  $v_{\text{bc}} = 1\sigma_{v_{\text{bc}}}$ .

In summary, at least a  $8 h^{-1}$  Mpc box is necessary to capture the atomic cooling regime in the case with the streaming velocity, while even a larger box is necessary in the case without the streaming velocity. This might be one of the reasons why the second peak was not observed in previous semi-analytic studies that used much smaller boxes (e.g.,  $2 h^{-1}$  Mpc for Visbal et al. 2020).

#### 4.4. Impact of the spatial variation of LW feedback

Many previous studies adopted spatially uniform LW background (e.g., Hartwig et al. 2022; Hegde & Furlanetto 2023; Bovill et al. 2024; Feathers et al. 2024; Ventura et al. 2024), while others took the spatial variation into account (e.g., Agarwal et al. 2012; Visbal et al. 2020) within a few  $h^{-1}$  Mpc simulation box. However, it is essential to use a larger box to investigate the effect of inhomogeneous LW background because spatial inhomogeneities could dominate the intensity up to a distance of  $\sim 100$  proper kpc (Incatasciato et al.

2023). In this paper, we first examine the impact of the spatial variation of LW feedback within much larger spatial volume compared to the previous studies.

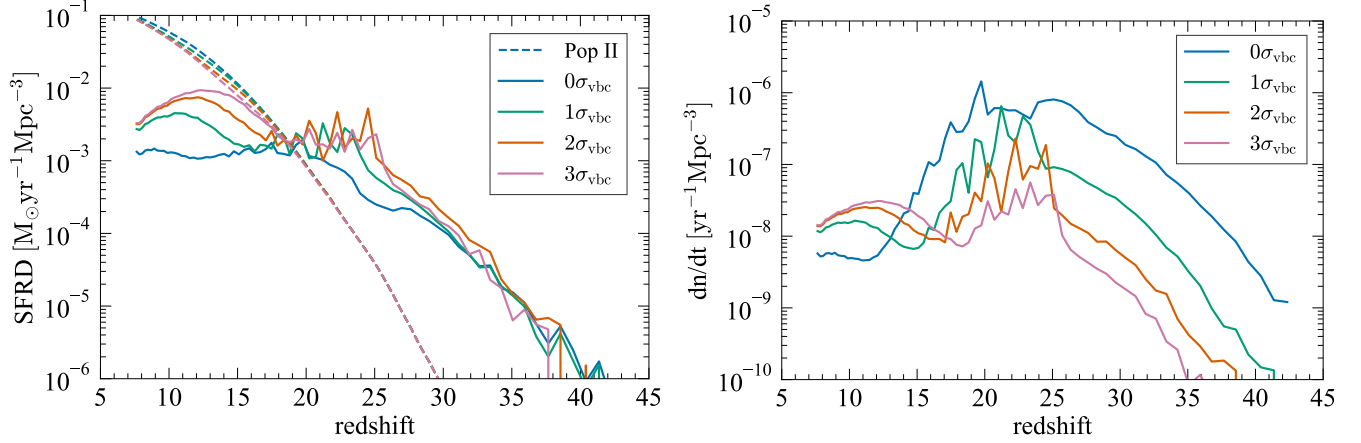
In our self-consistent model, the spatial variation of LW feedback naturally emerges. We compare it with a model adopting spatially uniform LW background. To compute the uniform background, we follow the formulae in Greif & Bromm (2006),

$$J_{\text{LW}}(z) \simeq \frac{hc}{4\pi m_{\text{H}}} \eta_{\text{LW}} \rho_{\star}(z) (1+z)^3, \quad (17)$$

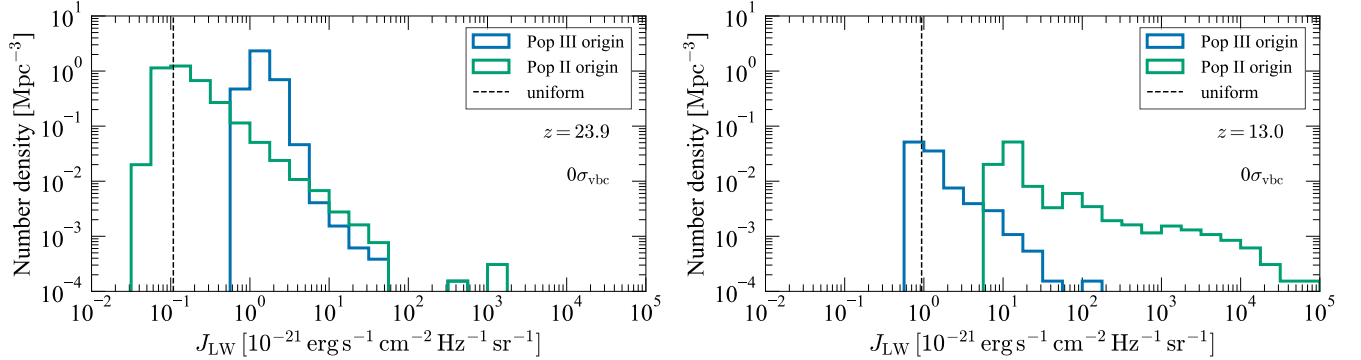
where,  $h$ ,  $c$ , and  $m_{\text{H}}$  are the Planck constant, speed of light, and hydrogen atom mass, respectively. The constant  $\eta_{\text{LW}}$  denotes the number of LW photon products per stellar baryon; here we assume  $\eta_{\text{LW}} \simeq 10^4$  and  $2 \times 10^4$  for Pop III and II stars, respectively. We evaluate  $\rho_{\star}(z)$  every step directly during model calculations, which is the comoving mass density of living Pop III stars and Pop II stars formed within 5 Myr from the current substep as used in Eq (16).

Figure 8 shows the comparison of self-consistent and spatially uniform LW models on the Phi-4096 simulation for the  $v_{\text{bc}} = 1\sigma_{v_{\text{bc}}}$  case. Both models give a similar formation rate of minihalos at  $z \gtrsim 30$  (bottom panel), while it changes dramatically after that, which corresponds to the epoch that Pop II SFRD starts to rise. At that time, the *spatially average* LW background does not grow sufficiently (see also Figure 1 and 6), therefore, the formation rate is not suppressed in the uniform model. On the other hand, the Pop III formation in minihalos near to Pop II-forming halos starts to be suppressed effectively due to the *locally strong* LW background in the self-consistent model. This suppression gradually becomes strong and the formation rate is reduced by a factor of  $\sim 10$  and  $100$  at  $z \sim 20$  and  $15$ , respectively. The second peak emerges in the self-consistent model at  $z < 15$ . This is not observed in the uniform model although the average formation rate is gradually suppressed due to a well-grown uniform LW background at  $z < 15$ . As already seen in section 4.3, at least a  $8 h^{-1}$  Mpc box is necessary to correctly capture the atomic cooling regime in the case with the streaming velocity. Our results shown here indicate that the self-consistent model is also necessary to capture it.

Intriguingly, the SFRD of Pop III stars is similar between both models before the second peak. This can be understood as follows. In the uniform model, most of the minihalos are not radiated by enough LW photons from nearby sources to photodissociate  $\text{H}_2$  molecules within them, therefore, the typical minihalo mass (and also Pop III mass) is smaller than that of the self-consistent model. In fact, the Pop III mass plot shows that the uniform model gives a number of low-mass Pop III stars and even the HD cooling mode ( $M_{\text{III}} \lesssim 10^2 M_{\odot}$ ) emerges, which is not observed in the self-consistent model regardless of the value of streaming velocity, as discussed in



**Figure 5.** (Left) Star formation rate density (SFRD) of Pop III (solid curves) and Pop II (dashed) stars. Four model results with the different values of streaming velocity,  $v_{bc} = 0, 1\sigma_{vbc}, 2\sigma_{vbc},$  and  $3\sigma_{vbc}$ , are shown. (Right) Formation rate density of Pop III-forming minihalos per  $\text{Mpc}^3$  and year.



**Figure 6.** Number density of Pop III stars as a function of the Lyman-Werner flux radiated on their halos at  $z = 23.9$  (left) and  $z = 13.0$  (right) for  $v_{bc} = 0$  model. Histograms show  $J_{LW}$  from Pop III and Pop II sources in the fiducial (self-consistent) model. We divide a single-digit  $J_{LW}$  range into four logarithmic bins and calculate the number density in each bin. Vertical dashed lines show results from the spatially uniform  $J_{LW}$  model.

section 4.1. The difference of typical Pop III mass results in the similar Pop III SFRD at  $z \gtrsim 15$ .

## 5. DISCUSSIONS

### 5.1. Implications for the formation of supermassive black holes at high redshift

In this section, we discuss whether the supermassive Pop III stars can be a promising candidate of the seed of supermassive black holes (SMBHs) by comparing the number density of these stars with that of high- $z$  QSOs. The global average number density of supermassive stars per comoving  $\text{Mpc}^3$  ( $n_{\text{SMS}}$ ) predicted in the four models is shown in Table 2. Assuming each of 20, 72, 8, and 0% of the whole volume is the spatial region with the streaming velocity of  $v_{bc} = 0, 1\sigma_{vbc}, 2\sigma_{vbc},$  and  $3\sigma_{vbc}$ , respectively, the number density of supermassive stars is predicted to be 9.54 and 5.23 per comoving  $\text{Mpc}^3$  for  $M_{\text{III}} > 10^4$  and  $10^5 M_{\odot}$ , respectively. The existence of streaming velocity enhances the global number of supermassive stars by a factor of 1.6~2.6.

The number density estimated above is the global average. The high- $z$  QSOs should be hosted by massive halos at that era, therefore, we next estimate the average number of supermassive stars per massive halo by counting the number of progenitor halos where supermassive Pop III stars with  $M_{\text{III}} > 10^4$  and  $10^5 M_{\odot}$  are born. Figure 9 shows the average number of supermassive stars accreted by a halo ( $\bar{N}_{\text{SMS}}$ ) as a function of halo virial mass at  $z = 7.5$ . Without the streaming velocity, the number of supermassive stars is unity in halos with  $0.9 \sim 4 \times 10^9 M_{\odot}$  virial mass. Intriguingly, this mass is quite similar with the prediction by Chiaki et al. (2023), which performed a similar semi-analytic calculation on several regions from cosmological zoom-in simulations, although the model details are quite different. On the other hand, taking the streaming velocity into account, the number of supermassive stars is unity for  $0.4 \sim 1 \times 10^9 M_{\odot}$ , which is a factor of 2~4 less massive than the case without the streaming velocity. Cosmological hydrodynamical simulations suggest that a halo with the mass of several  $10^9 M_{\odot}$  and a BH seed

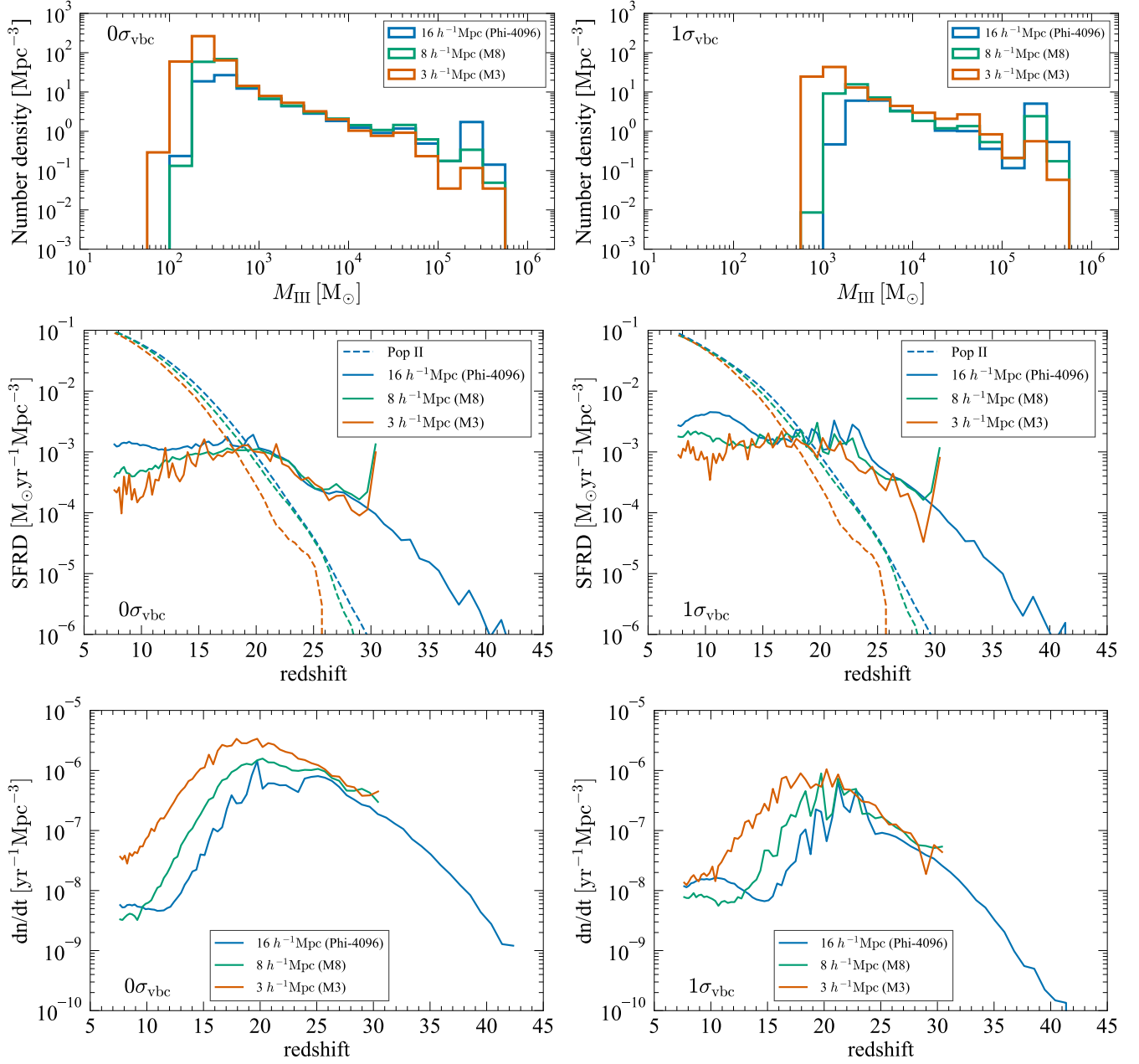


**Figure 7.** Comparison of model results calculated on simulations with different box sizes (16, 8, and  $3 h^{-1} \text{Mpc}$  for Phi-4096, M8, and M3, respectively). Left and right three panels show results of the model with  $v_{\text{bc}} = 0$  and  $1\sigma_{v_{\text{bc}}}$ , respectively. (Top) Number density of Pop III stars across redshift as a function of the Pop III mass in a halo, same as Figure 3. (Middle) Star formation rate density, same as Figure 5. (Bottom) Formation rate density of Pop III-forming minihalos, same as Figure 5.

with  $10^{4-6} M_{\odot}$  can produce a QSO at  $z = 6$  (Bhowmick et al. 2022), which is consistent with our results.

Arita et al. (2023) estimated that the halo mass of QSOs at  $z \sim 6$  is about  $5.0 \times 10^{12} h^{-1} M_{\odot}$  using clustering analysis of spectroscopically identified QSOs. In our simulation, we do not have halos with such mass at  $z = 7.5$  due to the limiting size of simulation volume. Extrapolating the result in Figure 9, a number of supermassive stars could be hosted by such halos as halos merge with each other into more massive

halos. Some of the stars could also merge with each other to form SMBHs, and the others can orbit within a main halo. We do not consider mergers of stars (or BHs) in the current model and plan to investigate this in future work. Future observations is also essential to further constrain the Pop III formation scenario (e.g., Shirakata et al. 2016; Matsuoka et al. 2023; Oogi et al. 2023).

## 5.2. Single or multiple Pop III formation scenario

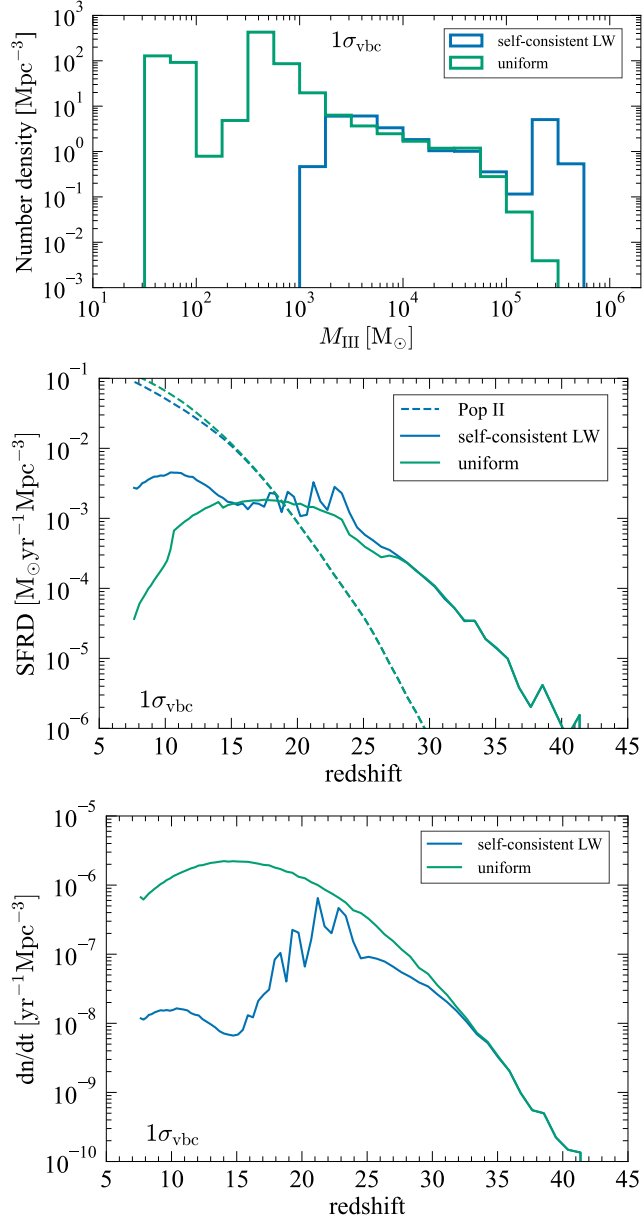


**Figure 8.** Comparison of different implementations of the LW feedback on the Phi-4096 simulation for the  $v_{bc} = 1\sigma_{vbc}$  case. Blue and green curves show results of the fiducial (self-consistent) model and spatially uniform  $J_{LW}$  model, respectively. (Top) Number density of Pop III stars across redshift as a function of the Pop III mass in a halo, same as Figure 3. (Middle) Star formation rate density, same as Figure 5. (Bottom) Formation rate density of Pop III-forming minihalos, same as Figure 5.

In this study, we have assumed that a single Pop III stars is born within a minihalo. However, recent radiative hydrodynamical simulations showed that massive Pop III binary stars can be born as a result of fragmentation of circumstellar disks in the vicinity of Pop III due to the gravitational instability (Sugimura et al. 2020). The total mass of individual stars

**Table 2.** Global average number density of supermassive stars per comoving  $\text{Mpc}^3$  ( $n_{\text{SMS}}$ ) for the four models. The integration results across the streaming velocity are shown in the bottom row (labelled “combine”), where each of 20, 72, 8, and 0% of the whole volume is assumed to be the spatial region with the streaming velocity of  $v_{bc} = 0, 1\sigma_{vbc}, 2\sigma_{vbc},$  and  $3\sigma_{vbc}$ , respectively.

$\sigma_{vbc}$	$n_{\text{SMS}}$ ( $M_{\text{III}} > 10^4 M_{\odot}$ )	$n_{\text{SMS}}$ ( $M_{\text{III}} > 10^5 M_{\odot}$ )
0	5.85	2.04
1	9.96	5.71
2	14.93	8.87
3	12.53	10.76
combine	9.54	5.23

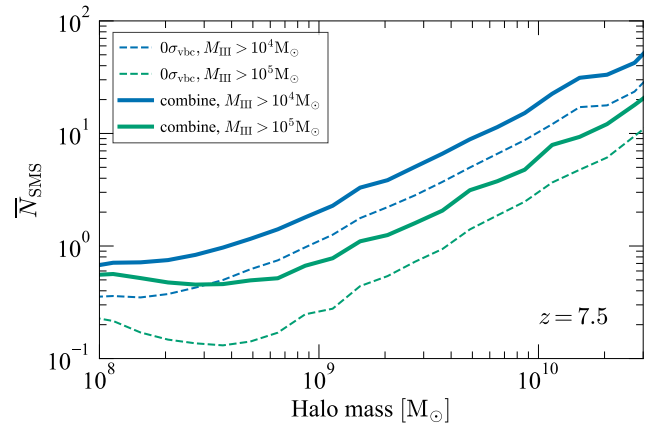


**Figure 9.** Average number of supermassive stars per halo ( $\bar{N}_{\text{SMS}}$ ) as a function of halo virial mass at  $z = 7.5$ . Blue and green curves show the results for  $M_{\text{III}} > 10^4$  and  $10^5 M_{\odot}$ , respectively. Thin and thick curves show the results for  $0\sigma_{vbc}$  and the combination of four models, respectively (details are provided in the text and Table 2 caption).

in their simulations is consistent with single star simulations (Sugimura et al. 2023). Therefore, the Pop III mass predicted by our model can be interpreted as an upper limit of that per minihalo.

Another possibility is the formation of Pop III clusters as shown by radiative hydrodynamical simulations (Hirano et al. 2018, 2023). As the value of initial streaming velocity increases, the morphology of the massive gas cloud in a halo becomes more asymmetric; hence, the fragmentation of massive gas can occur more easily. In their simulations, the maximum of four dense gas clouds can form simultaneously.

A cosmological magnetic field can also impact the formation of Pop III stars. Magnetohydrodynamic simulations showed that the dynamo effect can exponentially amplify the cosmological magnetic field strength around the Pop III protostars and then prevent disk fragmentation, resulting in the formation of single massive star (Hirano & Machida 2022; Higashi et al. 2024).

Overall, there is no consensus about the multiplicity of the Pop III formation at this moment, and therefore, we have assumed that a single Pop III star is born within a minihalo throughout this work. We will investigate this issue in our future work.

## 6. SUMMARY

In this paper, we have developed a new semi-analytic framework of Pop III stars and subsequent galaxy formation designed to run on halo merger trees. In our framework, the critical minihalo mass for the Pop III formation depends on the LW flux from Pop III and II sources and the dark matter baryon streaming velocity, motivated by results of recent radiative hydrodynamical simulations. The Pop III mass is also modelled as reproducing simulation results, taking the formation of supermassive stars into account. Our model incorporates the LW feedback in a self-consistent way, and therefore, the spatial variation of LW feedback naturally emerges. We also conducted a high-resolution cosmological simulation with the box size of  $16 h^{-1} \text{Mpc}$  having enough mass resolution to resolve Pop III-forming minihalos, which is a much larger volume than that adopted in previous studies using semi-analytic models and radiative hydrodynamical simulations. We have combined this simulation with the semi-analytic framework and investigated the Pop III IMF and SFRD of Pop III and II from  $z = 43$  to  $7.5$ . The results are summarized as follows.

1. The IMF of Pop III stars is top-heavy and two peaks in the distribution exist. The first peak is around the less massive end, which corresponds to the  $\text{H}_2$  cooling halos, while the second peak corresponds to the atomic cooling halos, where supermassive stars can be born. The Pop III mass at the first peak increases with the value of streaming velocity because the critical halo mass of Pop III-forming halos also increases. The mass of the second peak is  $\sim 2 \times 10^5 M_\odot$  in our model regardless of the value of streaming velocity. The fractions of such supermassive stars are about 2, 21, 57, and 83% for  $v_{\text{bc}} = 0, 1\sigma_{\text{vbc}}, 2\sigma_{\text{vbc}},$  and  $3\sigma_{\text{vbc}}$ , respectively.
2. Regardless of the value of streaming velocity, the corresponding redshift and LW flux of the first peak on the IMF are around  $20 \lesssim z \lesssim 25$  and  $J_{\text{LW}} \lesssim 10$ , respectively. The second peak exists around  $7.5 \lesssim z \lesssim 15$  and  $J_{\text{LW}} \gtrsim 10$ . As the value of streaming velocity increases, the second peaks emerge from slightly higher

redshift and the number density of Pop III therein also increases.

3. The Pop III formation begins around  $z \sim 40$ , and the formation rate (in terms of the number of Pop III-forming minihalos) rises with evolving redshift and reaches the first peak at  $20 \lesssim z \lesssim 25$ . Around this redshift, LW flux sufficiently grows to prevent subsequent Pop III formation. The formation rate rises again and reaches the second peak around  $7.5 \lesssim z \lesssim 15$  as new Pop III stars are born in atomic cooling halos, which is also seen in SFRD. The Pop III SFRD is higher with increasing streaming velocity, while the formation rate density of Pop III-forming halos shows the opposite sense in the  $\text{H}_2$  cooling regime. In contrast, in the atomic cooling regime, both the SFRD and Pop III-forming halo formation rate are higher with increasing streaming velocity.
4. To incorporate LW feedback sufficiently from surrounding Pop II stars and capture the atomic cooling regime, at least an  $8 h^{-1} \text{Mpc}$  simulation box is necessary in the case with the streaming velocity, while even a larger box is necessary in the case without the streaming velocity. A model adopting spatially uniform LW background used in many previous literatures can not capture the atomic cooling regime, therefore, the self-consistent model used in this paper is necessary to correctly model Pop III stars in the atomic cooling halos.
5. Our model predicts one supermassive star per halo with several  $10^9 M_\odot$  at  $z=7.5$ , which is enough to reproduce a high redshift quasar.

- 1 This work has been supported by IAAR Research Support
- 2 Program in Chiba University Japan, MEXT/JSPS KAKENHI
- 3 (Grant Number JP17H04828, JP19KK0344, JP21H01122
- 4 (T.I), JP21K13960, JP21H01123 (S.H)), MEXT as ‘‘Program
- 5 for Promoting Researches on the Supercomputer Fugaku’’
- 6 (JPMXP1020200109 and JPMXP1020230406), and JICFuS.
- 7 Numerical computations were carried out on Aterui-II su-
- 8 percomputer at the Center for Computational Astrophysics,
- 9 National Astronomical Observatory of Japan.

## REFERENCES

Abel, T., Bryan, G. L., & Norman, M. L. 2002, *Science*, 295, 93,

doi: [10.1126/science.295.5552.93](https://doi.org/10.1126/science.295.5552.93)

Agarwal, B., Khochfar, S., Johnson, J. L., et al. 2012, *MNRAS*,

425, 2854, doi: [10.1111/j.1365-2966.2012.21651.x](https://doi.org/10.1111/j.1365-2966.2012.21651.x)

- Arita, J., Kashikawa, N., Matsuoka, Y., et al. 2023, *ApJ*, 954, 210, doi: [10.3847/1538-4357/ace43a](https://doi.org/10.3847/1538-4357/ace43a)
- Becerra, F., Greif, T. H., Springel, V., & Hernquist, L. E. 2015, *MNRAS*, 446, 2380, doi: [10.1093/mnras/stu2284](https://doi.org/10.1093/mnras/stu2284)
- Behroozi, P. S., Wechsler, R. H., & Wu, H.-Y. 2013a, *ApJ*, 762, 109, doi: [10.1088/0004-637X/762/2/109](https://doi.org/10.1088/0004-637X/762/2/109)
- Behroozi, P. S., Wechsler, R. H., Wu, H.-Y., et al. 2013b, *ApJ*, 763, 18, doi: [10.1088/0004-637X/763/1/18](https://doi.org/10.1088/0004-637X/763/1/18)
- Bhowmick, A. K., Blecha, L., Ni, Y., et al. 2022, *MNRAS*, 516, 138, doi: [10.1093/mnras/stac2238](https://doi.org/10.1093/mnras/stac2238)
- Bovill, M. S., Stiavelli, M., Wiggins, A. I., Ricotti, M., & Trenti, M. 2024, *ApJ*, 962, 49, doi: [10.3847/1538-4357/ad148a](https://doi.org/10.3847/1538-4357/ad148a)
- Bromm, V., & Larson, R. B. 2004, *ARA&A*, 42, 79, doi: [10.1146/annurev.astro.42.053102.134034](https://doi.org/10.1146/annurev.astro.42.053102.134034)
- Bromm, V., & Loeb, A. 2003, *ApJ*, 596, 34, doi: [10.1086/377529](https://doi.org/10.1086/377529)
- Chiaki, G., Chon, S., Omukai, K., et al. 2023, *MNRAS*, 521, 2845, doi: [10.1093/mnras/stad689](https://doi.org/10.1093/mnras/stad689)
- Chon, S., Hirano, S., Hosokawa, T., & Yoshida, N. 2016, *ApJ*, 832, 134, doi: [10.3847/0004-637X/832/2/134](https://doi.org/10.3847/0004-637X/832/2/134)
- Clark, P. C., Glover, S. C. O., & Klessen, R. S. 2008, *ApJ*, 672, 757, doi: [10.1086/524187](https://doi.org/10.1086/524187)
- Clark, P. C., Glover, S. C. O., Klessen, R. S., & Bromm, V. 2011a, *ApJ*, 727, 110, doi: [10.1088/0004-637X/727/2/110](https://doi.org/10.1088/0004-637X/727/2/110)
- Clark, P. C., Glover, S. C. O., Smith, R. J., et al. 2011b, *Science*, 331, 1040, doi: [10.1126/science.1198027](https://doi.org/10.1126/science.1198027)
- Cole, S., Aragon-Salamanca, A., Frenk, C. S., Navarro, J. F., & Zepf, S. E. 1994, *MNRAS*, 271, 781, doi: [10.1093/mnras/271.4.781](https://doi.org/10.1093/mnras/271.4.781)
- Crocce, M., Pueblas, S., & Scoccimarro, R. 2006, *MNRAS*, 373, 369, doi: [10.1111/j.1365-2966.2006.11040.x](https://doi.org/10.1111/j.1365-2966.2006.11040.x)
- Feathers, C. R., Kulkarni, M., Visbal, E., & Hazlett, R. 2024, *ApJ*, 962, 62, doi: [10.3847/1538-4357/ad1688](https://doi.org/10.3847/1538-4357/ad1688)
- Fernandez, R., Bryan, G. L., Haiman, Z., & Li, M. 2014, *MNRAS*, 439, 3798, doi: [10.1093/mnras/stu230](https://doi.org/10.1093/mnras/stu230)
- Fialkov, A., Barkana, R., Tseliakhovich, D., & Hirata, C. M. 2012, *MNRAS*, 424, 1335, doi: [10.1111/j.1365-2966.2012.21318.x](https://doi.org/10.1111/j.1365-2966.2012.21318.x)
- Greif, T. H., & Bromm, V. 2006, *MNRAS*, 373, 128, doi: [10.1111/j.1365-2966.2006.11017.x](https://doi.org/10.1111/j.1365-2966.2006.11017.x)
- Greif, T. H., Bromm, V., Clark, P. C., et al. 2012, *MNRAS*, 424, 399, doi: [10.1111/j.1365-2966.2012.21212.x](https://doi.org/10.1111/j.1365-2966.2012.21212.x)
- Greif, T. H., Springel, V., White, S. D. M., et al. 2011, *ApJ*, 737, 75, doi: [10.1088/0004-637X/737/2/75](https://doi.org/10.1088/0004-637X/737/2/75)
- Griffen, B. F., Dooley, G. A., Ji, A. P., et al. 2018, *MNRAS*, 474, 443, doi: [10.1093/mnras/stx2749](https://doi.org/10.1093/mnras/stx2749)
- Hahn, O., & Abel, T. 2011, *MNRAS*, 415, 2101, doi: [10.1111/j.1365-2966.2011.18820.x](https://doi.org/10.1111/j.1365-2966.2011.18820.x)
- Haiman, Z., Thoul, A. A., & Loeb, A. 1996, *ApJ*, 464, 523, doi: [10.1086/177343](https://doi.org/10.1086/177343)
- Harikane, Y., Ouchi, M., Oguri, M., et al. 2023, *ApJS*, 265, 5, doi: [10.3847/1538-4365/acaaa9](https://doi.org/10.3847/1538-4365/acaaa9)
- Hartwig, T., Bromm, V., Klessen, R. S., & Glover, S. C. O. 2015, *MNRAS*, 447, 3892, doi: [10.1093/mnras/stu2740](https://doi.org/10.1093/mnras/stu2740)
- Hartwig, T., Magg, M., Chen, L.-H., et al. 2022, *ApJ*, 936, 45, doi: [10.3847/1538-4357/ac7150](https://doi.org/10.3847/1538-4357/ac7150)
- Hegde, S., & Furlanetto, S. R. 2023, *MNRAS*, 525, 428, doi: [10.1093/mnras/stad2308](https://doi.org/10.1093/mnras/stad2308)
- Higashi, S., Susa, H., Federrath, C., & Chiaki, G. 2024, *ApJ*, 962, 158, doi: [10.3847/1538-4357/ad2066](https://doi.org/10.3847/1538-4357/ad2066)
- Hirano, S., Hosokawa, T., Yoshida, N., Omukai, K., & Yorke, H. W. 2015, *MNRAS*, 448, 568, doi: [10.1093/mnras/stv044](https://doi.org/10.1093/mnras/stv044)
- Hirano, S., Hosokawa, T., Yoshida, N., et al. 2014, *ApJ*, 781, 60, doi: [10.1088/0004-637X/781/2/60](https://doi.org/10.1088/0004-637X/781/2/60)
- Hirano, S., & Machida, M. N. 2022, *ApJL*, 935, L16, doi: [10.3847/2041-8213/ac85e0](https://doi.org/10.3847/2041-8213/ac85e0)
- Hirano, S., Shen, Y., Nishijima, S., Sakai, Y., & Umeda, H. 2023, *MNRAS*, 525, 5737, doi: [10.1093/mnras/stad2693](https://doi.org/10.1093/mnras/stad2693)
- Hirano, S., Yoshida, N., Sakurai, Y., & Fujii, M. S. 2018, *ApJ*, 855, 17, doi: [10.3847/1538-4357/aaaaba](https://doi.org/10.3847/1538-4357/aaaaba)
- Hosokawa, T., Omukai, K., Yoshida, N., & Yorke, H. W. 2011, *Science*, 334, 1250, doi: [10.1126/science.1207433](https://doi.org/10.1126/science.1207433)
- Inayoshi, K., Omukai, K., & Tasker, E. 2014, *MNRAS*, 445, L109, doi: [10.1093/mnras/slu151](https://doi.org/10.1093/mnras/slu151)
- Inayoshi, K., Visbal, E., & Haiman, Z. 2020, *ARA&A*, 58, 27, doi: [10.1146/annurev-astro-120419-014455](https://doi.org/10.1146/annurev-astro-120419-014455)
- Incatasciato, A., Khochfar, S., & Oñorbe, J. 2023, *MNRAS*, 522, 330, doi: [10.1093/mnras/stad1008](https://doi.org/10.1093/mnras/stad1008)
- Ishiyama, T., Fukushige, T., & Makino, J. 2009, *PASJ*, 61, 1319, doi: [10.1093/pasj/61.6.1319](https://doi.org/10.1093/pasj/61.6.1319)
- Ishiyama, T., Nitadori, K., & Makino, J. 2012, in *Proc. Int. Conf. High Performance Computing, Networking, Storage and Analysis, SC'12* (Los Alamitos, CA: IEEE Computer Society Press), 5:, (arXiv:1211.4406). <http://dl.acm.org/citation.cfm?id=2388996.2389003>
- Ishiyama, T., Sudo, K., Yokoi, S., et al. 2016, *ApJ*, 826, 9, doi: [10.3847/0004-637X/826/1/9](https://doi.org/10.3847/0004-637X/826/1/9)
- Ishiyama, T., Prada, F., Klypin, A. A., et al. 2021, *MNRAS*, 506, 4210, doi: [10.1093/mnras/stab1755](https://doi.org/10.1093/mnras/stab1755)
- Johnson, J. L., Dalla Vecchia, C., & Khochfar, S. 2013, *MNRAS*, 428, 1857, doi: [10.1093/mnras/sts011](https://doi.org/10.1093/mnras/sts011)
- Kauffmann, G., Colberg, J. M., Diaferio, A., & White, S. D. M. 1999, *MNRAS*, 303, 188, doi: [10.1046/j.1365-8711.1999.02202.x](https://doi.org/10.1046/j.1365-8711.1999.02202.x)
- Kinugawa, T., Inayoshi, K., Hotokezaka, K., Nakauchi, D., & Nakamura, T. 2014, *MNRAS*, 442, 2963, doi: [10.1093/mnras/stu1022](https://doi.org/10.1093/mnras/stu1022)
- Kirihara, T., Hasegawa, K., Umemura, M., Mori, M., & Ishiyama, T. 2020, *MNRAS*, 491, 4387, doi: [10.1093/mnras/stz3376](https://doi.org/10.1093/mnras/stz3376)
- Kirihara, T., Susa, H., Hosokawa, T., & Kinugawa, T. 2023, *ApJ*, 950, 188, doi: [10.3847/1538-4357/acd1e0](https://doi.org/10.3847/1538-4357/acd1e0)



- Kirihara, T., Tanikawa, A., & Ishiyama, T. 2019, *MNRAS*, 486, 5917, doi: [10.1093/mnras/stz1277](https://doi.org/10.1093/mnras/stz1277)
- Kulkarni, M., Visbal, E., & Bryan, G. L. 2021, *ApJ*, 917, 40, doi: [10.3847/1538-4357/ac08a3](https://doi.org/10.3847/1538-4357/ac08a3)
- Lewis, A., Challinor, A., & Lasenby, A. 2000, *ApJ*, 538, 473, doi: [10.1086/309179](https://doi.org/10.1086/309179)
- Machida, M. N., & Doi, K. 2013, *MNRAS*, 435, 3283, doi: [10.1093/mnras/stt1524](https://doi.org/10.1093/mnras/stt1524)
- Magg, M., Hartwig, T., Agarwal, B., et al. 2018, *MNRAS*, 473, 5308, doi: [10.1093/mnras/stx2729](https://doi.org/10.1093/mnras/stx2729)
- Matsuoka, Y., Onoue, M., Iwasawa, K., et al. 2023, *ApJL*, 949, L42, doi: [10.3847/2041-8213/acd69f](https://doi.org/10.3847/2041-8213/acd69f)
- Nishi, R., & Susa, H. 1999, *ApJL*, 523, L103, doi: [10.1086/312277](https://doi.org/10.1086/312277)
- Nishijima, S., Hirano, S., & Umeda, H. 2024, *ApJ*, 965, 141, doi: [10.3847/1538-4357/ad2fc9](https://doi.org/10.3847/1538-4357/ad2fc9)
- Nitadori, K., Makino, J., & Hut, P. 2006, *NewA*, 12, 169, doi: [10.1016/j.newast.2006.07.007](https://doi.org/10.1016/j.newast.2006.07.007)
- Omukai, K., & Nishi, R. 1998, *ApJ*, 508, 141, doi: [10.1086/306395](https://doi.org/10.1086/306395)
- Omukai, K., & Palla, F. 2001, *ApJL*, 561, L55, doi: [10.1086/324410](https://doi.org/10.1086/324410)
- . 2003, *ApJ*, 589, 677, doi: [10.1086/374810](https://doi.org/10.1086/374810)
- Oogi, T., Ishiyama, T., Prada, F., et al. 2023, *MNRAS*, 525, 3879, doi: [10.1093/mnras/stad2401](https://doi.org/10.1093/mnras/stad2401)
- Planck Collaboration, Aghanim, N., Akrami, Y., et al. 2020, *A&A*, 641, A6, doi: [10.1051/0004-6361/201833910](https://doi.org/10.1051/0004-6361/201833910)
- Schaerer, D. 2002, *A&A*, 382, 28, doi: [10.1051/0004-6361:20011619](https://doi.org/10.1051/0004-6361:20011619)
- Shirakata, H., Kawaguchi, T., Okamoto, T., et al. 2016, *MNRAS*, 461, 4389, doi: [10.1093/mnras/stw1798](https://doi.org/10.1093/mnras/stw1798)
- Smith, R. J., Glover, S. C. O., Clark, P. C., Greif, T., & Klessen, R. S. 2011, *MNRAS*, 414, 3633, doi: [10.1111/j.1365-2966.2011.18659.x](https://doi.org/10.1111/j.1365-2966.2011.18659.x)
- Sugimura, K., Matsumoto, T., Hosokawa, T., Hirano, S., & Omukai, K. 2020, *ApJL*, 892, L14, doi: [10.3847/2041-8213/ab7d37](https://doi.org/10.3847/2041-8213/ab7d37)
- . 2023, *ApJ*, 959, 17, doi: [10.3847/1538-4357/ad02fc](https://doi.org/10.3847/1538-4357/ad02fc)
- Susa, H. 2013, *ApJ*, 773, 185, doi: [10.1088/0004-637X/773/2/185](https://doi.org/10.1088/0004-637X/773/2/185)
- . 2019, *ApJ*, 877, 99, doi: [10.3847/1538-4357/ab1b6f](https://doi.org/10.3847/1538-4357/ab1b6f)
- Susa, H., Hasegawa, K., & Tominaga, N. 2014, *ApJ*, 792, 32, doi: [10.1088/0004-637X/792/1/32](https://doi.org/10.1088/0004-637X/792/1/32)
- Tanaka, T., & Hasegawa, K. 2021, *MNRAS*, 502, 463, doi: [10.1093/mnras/stab072](https://doi.org/10.1093/mnras/stab072)
- Tanikawa, A., Yoshikawa, K., Nitadori, K., & Okamoto, T. 2013, *NewA*, 19, 74, doi: [10.1016/j.newast.2012.08.009](https://doi.org/10.1016/j.newast.2012.08.009)
- Tanikawa, A., Yoshikawa, K., Okamoto, T., & Nitadori, K. 2012, *NewA*, 17, 82, doi: [10.1016/j.newast.2011.07.001](https://doi.org/10.1016/j.newast.2011.07.001)
- Toyouchi, D., Inayoshi, K., Li, W., Haiman, Z., & Kuiper, R. 2023, *MNRAS*, 518, 1601, doi: [10.1093/mnras/stac3191](https://doi.org/10.1093/mnras/stac3191)
- Trinca, A., Schneider, R., Valiante, R., et al. 2024, *MNRAS*, 529, 3563, doi: [10.1093/mnras/stae651](https://doi.org/10.1093/mnras/stae651)
- Tseliakhovich, D., Barkana, R., & Hirata, C. M. 2011, *MNRAS*, 418, 906, doi: [10.1111/j.1365-2966.2011.19541.x](https://doi.org/10.1111/j.1365-2966.2011.19541.x)
- Tseliakhovich, D., & Hirata, C. 2010, *PhRvD*, 82, 083520, doi: [10.1103/PhysRevD.82.083520](https://doi.org/10.1103/PhysRevD.82.083520)
- Ventura, E. M., Qin, Y., Balu, S., & Wyithe, J. S. B. 2024, *MNRAS*, 529, 628, doi: [10.1093/mnras/stae567](https://doi.org/10.1093/mnras/stae567)
- Visbal, E., Bryan, G. L., & Haiman, Z. 2020, *ApJ*, 897, 95, doi: [10.3847/1538-4357/ab994e](https://doi.org/10.3847/1538-4357/ab994e)
- Visbal, E., Haiman, Z., & Bryan, G. L. 2018, *MNRAS*, 475, 5246, doi: [10.1093/mnras/sty142](https://doi.org/10.1093/mnras/sty142)
- Yoshida, N., Abel, T., Hernquist, L., & Sugiyama, N. 2003, *ApJ*, 592, 645, doi: [10.1086/375810](https://doi.org/10.1086/375810)
- Yoshida, N., Omukai, K., & Hernquist, L. 2008, *Science*, 321, 669, doi: [10.1126/science.1160259](https://doi.org/10.1126/science.1160259)
- Yoshida, N., Omukai, K., Hernquist, L., & Abel, T. 2006, *ApJ*, 652, 6, doi: [10.1086/507978](https://doi.org/10.1086/507978)
- Yoshikawa, K., & Tanikawa, A. 2018, *Research Notes of the American Astronomical Society*, 2, 231, doi: [10.3847/2515-5172/aaf7a2](https://doi.org/10.3847/2515-5172/aaf7a2)

## APPENDIX

## A. EFFECT OF MASS RESOLUTION

In this appendix, we examine the effect of the mass resolution of simulations on the IMF of Pop III stars across redshift and SFRD. Figure A1 shows the comparison of model results calculated on simulations with different mass resolutions (H3, M3, and L3), which are  $6.41 \times 10^2$ ,  $5.13 \times 10^3$ , and  $1.73 \times 10^4 h^{-1} M_\odot$ . The resolution of M3 is the same as the fiducial resolution, while that of L3 is the lowest and similar to those used in other semi-analytic studies (Magg et al. 2018; Griffen et al. 2018). The results with  $v_{bc} = 0$  (left panels) and  $1\sigma_{vbc}$  (right panels) are shown.

For the  $1\sigma_{vbc}$  case, three simulations give nearly converged results. For the  $v_{bc} = 0$  case, the H3 and M3 simulations agree with each other, although the middle-resolution simulation slightly overpredicts Pop III stars at the massive end. On the other hand, the L3 run underpredicts the formation rate of minihalos at  $z \gtrsim 15$  and slightly overpredicts it at  $z \lesssim 15$ , indicating that the mass resolution of L3 is not enough to resolve minihalos with the mass close to the smallest minihalo mass ( $\sim 10^5 h^{-1} M_\odot$ , see Figure 2). Because the mass of such minihalos exceeds the critical mass at a late time as they grow, the formation rate of minihalos at  $z \lesssim 15$  is slightly larger in lower resolution than in higher resolution simulations. As a result, the L3 run gives a larger number of massive stars and higher SFRD compared to the other runs for the  $v_{bc} = 0$  case. For the  $v_{bc} = 1\sigma_{vbc}$  case, this does not occur because the critical minihalo mass is always higher.

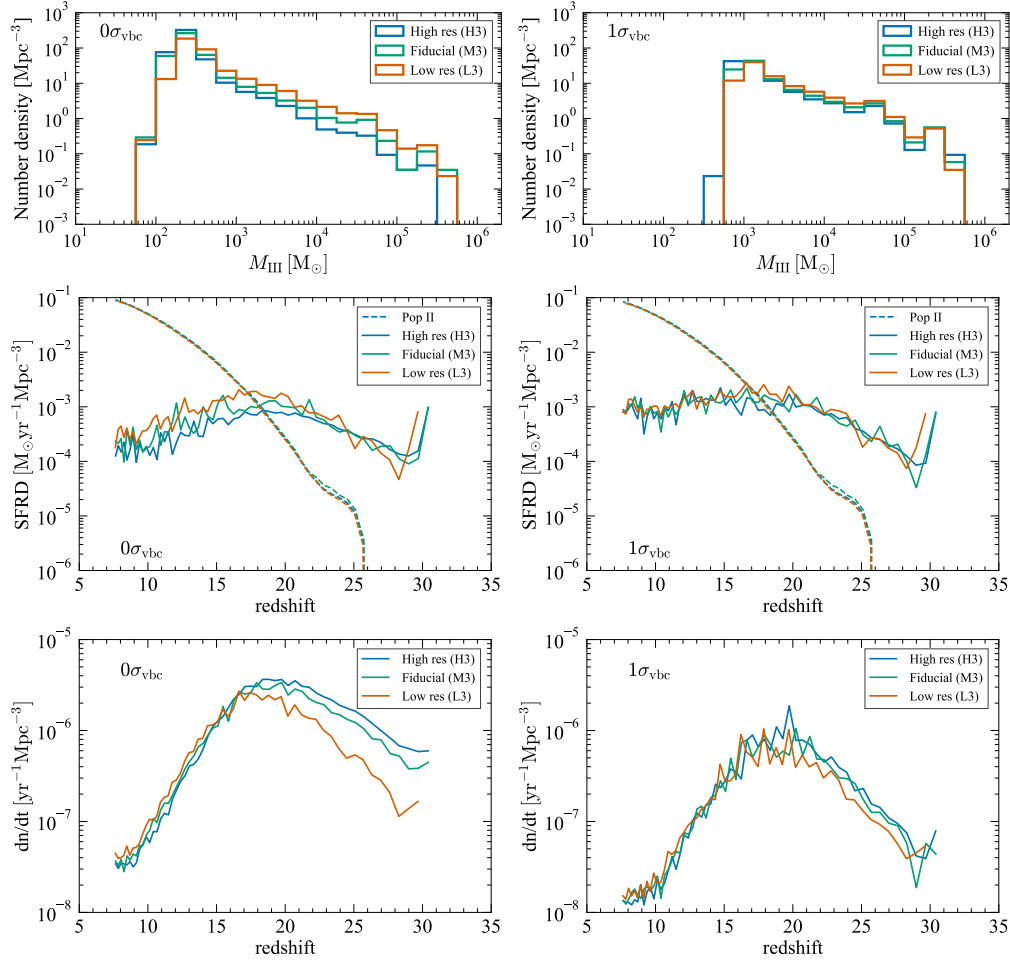


**Figure A1.** Comparison of model results calculated on simulations with different mass resolutions (H3, M3, and L3). Left and right three panels show results of model with  $v_{bc} = 0$  and  $1\sigma_{vbc}$ , respectively. (Top) Number density of Pop III stars across redshift as a function of the Pop III mass in a halo, same as Figure 3. (Middle) Star formation rate density, same as Figure 5. (Bottom) Formation rate density of Pop III-forming minihalos, same as Figure 5.